Article

A Multiscale Simulation Framework for Elucidating Photochemical Structure–Activity Relationships of Photoswitchable Ligands in Complex Biomolecular Environments

Amirhossein Bakhtiiari, Mohammad Khavani, Gustavo J. Costa, and Ruibin Liang*

Cite This: https://doi.org/10.1021/acs.jcim.5c01831

Read Online

ACCESS | 📊 Metrics & More | 📖 Article Recommendations | 🆂�1 Supporting Information

ABSTRACT: Predicting the photochemical structure–activity relationships (photo-SAR) of photoswitchable ligands in complex biomolecular environments remains a great challenge due to intricate protein–ligand interactions, strong electron correlation in multiple electronic states, coupled nuclear and electronic dynamics, and protein conformational flexibility. To bridge this gap, here we develop a unified multiscale simulation framework that integrates first-principles nonadiabatic dynamics, excited-state enhanced sampling, and ground-state alchemical free-energy calculations. We applied this approach to photostatins (PSTs), a class of photoswitchable tubulin inhibitors with promising light-regulated anticancer bioactivity, and validated our predictions against extensive experimental data, including ultrafast time-resolved crystallography, absorption spectra, and isomer-dependent bioactivity assays. Our simulations reveal, for the first time, that nonradiative decay rates correlate directly with equilibrium excited-state free-energy surfaces, which are modulated by substituents, protein electrostatics, and steric confinement. Specifically, protein electrostatic fields accelerate excited-state relaxation, whereas steric constraints oppose it. The balance of these factors determines the trend of excited-state dynamics across PST derivatives. Our results further show that the photoisomerization quantum yield depends on (1) the directional alignment of torsional motions with nonadiabatic coupling vectors during nonradiative decay, and (2) the propensity for backward ground-state isomerization, both of which are shaped by protein–ligand interactions. Finally, among the free-energy methods tested, thermodynamic integration most accurately captures subtle substituent effects on the contrast in binding affinities between isomers, a critical metric for minimizing their off-target effects in the dark-adapted state. This work establishes a robust computational platform for accurately predicting photodynamics and light-responsive binding affinities of photoswitchable ligands in biomolecular systems, while also providing novel mechanistic insights that can facilitate their rational design in biological and biomedical applications.

Multiscale Simulation Framework for Photo-SAR Prediction
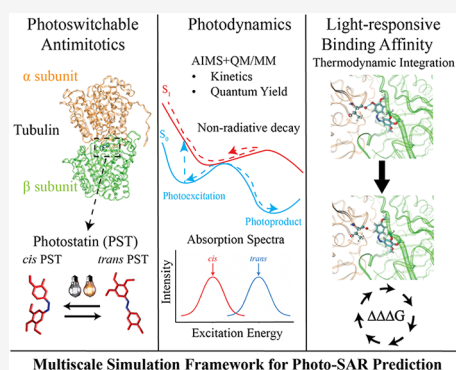
INTRODUCTION

Molecular photoswitches enable precise and reversible photocontrol of the structure and function of biomolecules, and have fundamentally transformed biological and biomedical research.[1−5] These compounds reversibly photoisomerize under specific wavelengths, and can also thermally relax to their most stable isomer form in the dark-adapted state. They are usually designed to mimic the nonphotochromic ligand of a biomolecular target (such as an enzyme or receptor), such that they can activate and inhibit the associated biochemical process locally with high spatial and temporal resolution via light. This unique advantage not only makes them useful probes to study cell signaling from a time-dependent perspective,[6,7] but also can be applied to reducing the severe side effects of traditional chemotherapy.[8−11] Previous experimental and computational studies have elucidated noticeable and complex effects of ligand-protein interactions on both the photoisomerization[12−15] and thermal isomerization[13,16,17] reactions of molecular photoswitches. To achieve high-

resolution photocontrol of protein function, it is essential to fine-tune their photochemical properties, such as absorption wavelength, isomerization rate, and quantum yield, while maximizing the difference in how distinct isomers of the same ligand interact with the biomolecular target.[5] A fundamental understanding of the photochemical structure–activity relationship (photo-SAR) of this class of compounds is thus necessary. However, previous studies have elucidated noticeable and complex effects of ligand-protein interactions on both the photoisomerization[12−15] and thermal isomerization[13,16,17] reactions of molecular photoswitches. This makes it significantly challenging to understand and predict how substituents

affect the photochemical properties and biochemical properties of molecular photoswitches in the biomolecular environments.

Despite advances in ultrafast time-resolved crystallography and spectroscopy,[15,18−22] directly probing the femto- to picosecond photodynamics of protein-bound photoswitches remains experimentally challenging. Molecular simulations can, in principle, unravel the ultrafast photodynamics of photoswitches in proteins with atomistic-level details, leading to a deep mechanistic understanding of how structural modifications and the embedding biomolecular environments modulate the kinetics and quantum yields of the photoreactions. However, such simulations are challenging for conventional quantum chemistry and molecular dynamics (MD) simulations.[5] First, the potential energy surfaces (PES) of both the ground and excited states, as well as their nonadiabatic couplings, must be accurately described by electronic structure methods incorporating both static and dynamic electron correlation. Second, the time-dependent Schrödinger's equation[23] must be solved by multistate nonadiabatic quantum dynamics approaches to propagate the coupled nuclear-electronic wave functions among electronic states that intersect one another. These challenges greatly hinder the accurate prediction of the photophysical and photochemical properties of molecular photoswitches in biomolecular environments, and thus their high-throughput computational design. Another major challenge is to accurately predict the substituents' effects on the binding affinity contrast between the *cis* and *trans* isomeric forms of photoswitches, which is critical for maximizing the light-responsiveness of the target's activity,[5] a key metric for achieving high-resolution photocontrol. Conventional computational approaches, such as docking simulations and standard molecular dynamics simulations, often struggle to accurately predict such properties.[5,24,25] All these challenges motivate us to develop, benchmark, and establish a robust multiscale simulation framework to predict the photo-SAR of molecular photoswitches in complex protein environments in this study. This is achieved by integrating nonadiabatic dynamics, first-principles electronic structure calculations, enhanced sampling, and alchemical free energy calculation techniques. This robust computational framework is extensively validated by various sources of experimental data, accurately quantifying the photo-SAR of this class of compounds. It thus holds great potential for advancing multiscale methods in computational chemistry and computer-aided designs of photoswitchable ligands in biomedical research.

Here, we benchmark this framework by applying it to investigate the photo-SAR of a diverse set of photostatins (PSTs) in tubulin, focusing on the effects of protein environment and substituents on the *cis*-to-*trans* photoisomerization and the contrast in *cis*-vs.-*trans* binding affinity of PSTs. The PSTs[8,9] are an emerging class of light-regulated anticancer therapeutics that were developed as photoswitchable analogs of combretastatin A-4 (CA4), which is known for its inhibitory effect on tubulin microtubule assembly[26] and has been in clinical trials for cancer treatment. Under illumination with ~400 nm light, the *cis* isomers of PSTs predominate, which bind at the colchicine-binding site lying at the interface between two tubulin subunits, thereby inhibiting tubulin polymerization.[15] In the absence of light or under illumination near 510 nm, the *trans* isomers predominate, weakening the PSTs' binding affinity with tubulin and lifting the inhibition.

Thus, the PSTs enable precise and reversible photocontrol over the mitosis and death of tumor cells.[8,9]

To date, rich experimental data have been accumulated on the absorption spectra, excited-state dynamics, time-resolved crystal structures, and the potency of various PSTs in different isomeric forms.[8,20,21,24,27] Notably, recent experiments[20,21] applied ultrafast time-resolved crystallography and transient absorption spectroscopy to resolve the time-dependent structural evolution of the PST1-tubulin complex arising from PST1's ultrafast *cis*-to-*trans* photoisomerization, and elucidated the photodynamics of the ligand and its subsequent release from the binding site with high resolution.[20,21] Despite these exciting experimental advancements, the molecular origins of how substituents and protein environments affect the photochemical properties and bioactivities of this class of photoswitches remain unclear. Therefore, the PST-tubulin complex presents an ideal benchmark system for validating our multiscale simulation framework. Meanwhile, a comprehensive computational investigation into this practically important yet challenging system will unravel the molecular origins underlying the design principles of molecular photoswitches for biomedical applications in general.

To address the challenges of simulating the photodynamics of the photoswitches, we employed the *ab initio* multiple spawning (AIMS) algorithm[28−31] to characterize the excited-state lifetime and quantum yields of the PST-derived photoswitches. The AIMS algorithm[28−31] is a nonadiabatic dynamics approach that efficiently solves the time-dependent Schrödinger equation and propagates the coupled electronic and nuclear degrees of freedom. Besides its computational efficiency, such an approach offers a unique advantage: it correctly decouples the nuclear and electronic degrees of freedom following nonadiabatic transitions, which usually necessitates *ad hoc* corrections for traditional nonadiabatic dynamics methods such as Ehrenfest and surface-hopping. In this study, we coupled AIMS with the hole−hole Tamm-Dancoff approximated density functional theory (hh-TDA-DFT) electronic structure method in a quantum mechanics/molecular mechanics (QM/MM) setting to calculate the potential energies, gradients, and nonadiabatic couplings of the system on-the-fly during the nonadiabatic dynamics simulation. The key advantage of the hh-TDA-DFT method is that it incorporates both static and dynamic electron correlation that are essential for predicting potential energy surfaces of photoswitches involving double-bond isomerizations.[12−14,16,32−34] This is because the use of a double-anion reference electron configuration allows coupling between ground and excited states by treating them on equal footing in the response formalism,[35] which is distinct from the time-dependent DFT method by construction. To accurately predict how substituent modifications alter the *cis*-vs.-*trans* binding affinity contrast, we benchmarked thermodynamic integration (TI) and molecular mechanics Poisson−Boltzmann surface area (MM/PBSA), two free energy methods widely used for *in silico* drug design, against the experimentally measured bioactivity (such as EC_{50}'s).[24,27]

In total, six PST derivatives, i.e., PST1, PST2, PST4, PST5, PST7, and PST27 (Figure 1), were investigated in this study, covering a variety of functional groups with different electronic and steric properties. These PSTs have been designed and characterized extensively in previous experimental studies.[8,9,20,21,24,27] Our results reveal opposite roles of protein electrostatics and steric restrictions in the photoisomerization

(A)

(B)
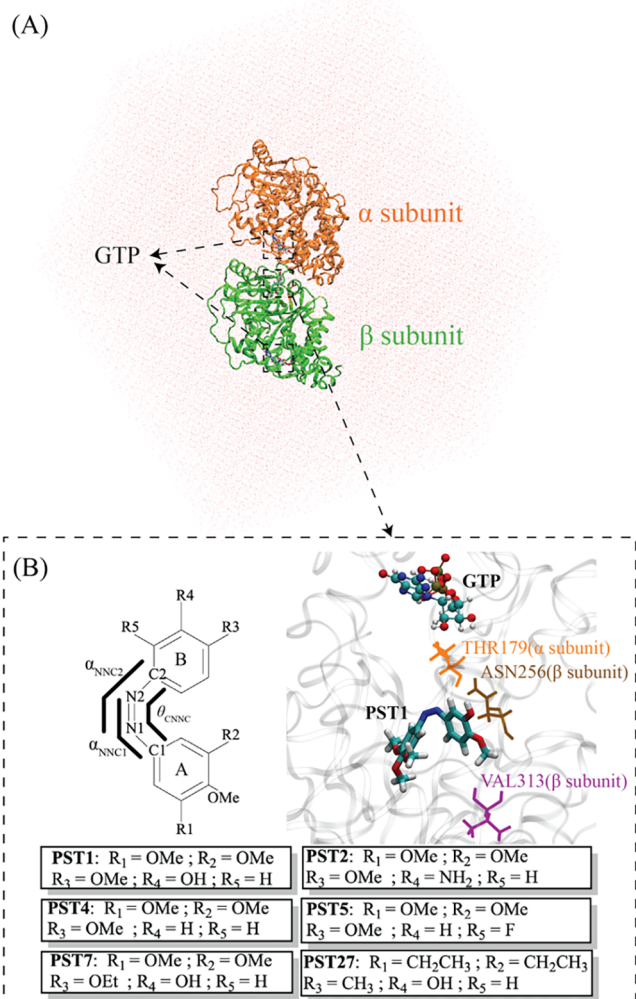
Figure 1. (A) Overview of the simulation system setup of tubulin complexed with PST derivatives. The α- and β-tubulin subunits are shown in orange and green, respectively, with the bound GTP and PST molecules indicated by dashed arrows. (B) Left: Chemical structures of the PST derivatives with defined R-group substitutions. The key bending angles α_{NNC2}, α_{NNC1} and torsion θ_{CNNC} are labeled. Right: binding pose of PST1 in the colchicine-binding site at the interface of α and β subunits (PDB ID: 8QL2), highlighting key residues interacting with PST1, including Thr179 (α subunit), Asn256, and Val313 (β subunit) residues.

dynamics while subtle electronic and steric perturbations significantly influence excited-state dynamics, quantum yields and binding affinities. The protein environment increases the isomerization quantum yield compared to the aqueous solution by reducing the ground-state backward isomerization. Among the tested free energy methods, only the TI method robustly captures the experimentally measured substituents' effect on the *cis*-vs.-*trans* binding affinity contrast. Bridging the gap between simulation and experimental measurements, this study establishes a predictive and robust computational framework capable of optimizing photochemical properties and light-responsive bioactivities.

■ **METHOD**

Below, we describe the detailed procedures of system setup, classical molecular mechanics (MM) MD equilibration simulations, ground-state QM/MM MD simulations, absorp-

tion spectra calculations, nonadiabatic excited-state dynamics using *ab initio* multiple spawning (AIMS), excited-state free energy simulation, TI simulation, and MM/PBSA simulation.

System Setup. The system setup started with the crystal structure of PST1 bound to tubulin (PDB: 8QL2). The crystal structure of PST1 was directly used for setting up the PST1-tubulin complex, while the initial structures of other PSTs were built by modifying PST1's substituents (Figure 1B). The following list of molecules was retained, while all the rest were removed: α and β subunits of tubulin, the bound GTP molecules along with the coordinating Mg^{2+} ions, crystal water molecules, and the PST. The missing residues in each subunit were added by homology modeling in MODELER software package.[36] The protonation states were assigned at pH = 6.5 by the H++ server.[37] The protein−ligand complex was then solvated in water molecules using the "LEap" program in the AmberTools20 package,[38] resulting in a periodic boundary condition (PBC) simulation box of ∼141 × 127 × 148 Å³ size and ∼220,000 atoms. The Na^+ ions were used to neutralize the net charge of the systems.

The protein and water molecules were modeled using the Amber ff14SB force field[39,40] and SPC/Fw model,[41] respectively. The force field parameters of each PST were assigned using the general AMBER Force Field (GAFF) approach.[42,43] Following our previous study,[16] the torsional terms for the central C−N═N−C dihedral (θ_{CNNC}) and the two neighboring C−C−N═N dihedrals (θ_{NNCC}) were reoptimized such that the MM PESs' obtained from the relaxed scans along these coordinates in the vacuum reproduce the QM PESs' using the hh-TDA-BH&HLYP/6-31G* method.[16] This reparameterization was crucial for preventing facile rotations of these torsions during the MD simulations, which would have otherwise been frequently observed using the default GAFF parameters. Parameters for the protein-bound GTP were obtained from a previous study.[44]

The setup of PST1, PST2, PST5, PST7, and PST27 in the aqueous solution and vacuum followed our previous study.[45] All classical MD simulations were performed using the AMBER20 software package.[46]

Classical MD Equilibration. Each PST-tubulin system was first subjected to energy minimization, applying harmonic restraints (500 kcal/mol/Å²) to the heavy atoms of the protein and crystal water molecules. Following this, a 100 ps MD simulation in the constant NVT ensemble at 300 K temperature was performed, using a reduced harmonic restraint of 50 kcal/mol/Å² on the same heavy atoms. Afterward, a 5 ns MD simulation in the constant NPT ensemble at 300 K temperature and 1 atm pressure was performed, while the force constants of the positional harmonic restraints were gradually reduced to zero. Subsequently, a 200 ns production simulation run was performed in the constant NPT ensemble at the same temperature and pressure without any external restraint. The temperature of the system was regulated by a Langevin thermostat (collision frequency: 1 ps⁻¹), while the pressure was regulated using the Berendsen barostat with a relaxation time constant of 1.0 ps. Throughout equilibration and production runs, an integration time step of 1 fs was used. The nonbonded cutoff distance for the van der Waals interactions was 10 Å, and the electrostatic interactions were calculated using the particle-mesh Ewald method.[47] All MM MD equilibration simulations were performed using the AMBER20 software package.[46]

C

Ground State QM/MM MD Equilibration. Following the MM MD simulations, QM/MM MD simulations were performed to correct geometric inaccuracies of the PST ligand described by the force field in order to prepare for the initial conditions (ICs) of the AIMS simulations.

For each PST-tubulin system, the last 80 ns of the constant NPT production simulation was used to extract 80 snapshots with a 1 ns time interval. From each snapshot, we extracted an open-boundary subsystem from the PBC simulation box. The subsystem excludes all water molecules and ions without any atoms within 5 Å of any atom of the protein. This truncation of the original system was mainly due to the limitations of the production version of the TeraChem software package[48−53] in treating the PBC condition of excited-state QM/MM calculations at the time of this study.

The ground-state QM/MM MD equilibration has the following settings. The QM region contains only the PST and was treated with the density functional theory using the BH&HLYP functional and 6-31G* basis set, i.e., BH&HLYP/6-31G*. The rest of the system, including the protein, solvent, GTP, and ions, was modeled using the MM force fields described above. An illustration of the QM/MM partitioning is included in Figure S8. This partitioning has been successfully applied in our previous study to investigate the effects of protein−ligand interaction on the ground-state isomerization kinetics of the PSTs[16] and computational studies of similar photoactive systems.[12−14,54] Electrostatic embedding was employed to solve the QM region's electronic structure in the presence of the MM region's fixed-point charges. Each QM/MM classical MD simulation was propagated with 0.5 fs time step for 3 ps in the constant NVT ensemble at 300 K temperature regulated by the Noose-Hover thermostat. The coordinates and velocities in the last snapshot of the QM/MM MD trajectory were used as the ICs for the AIMS simulations, resulting in 80 ICs for each of the five PST-tubulin systems.

Additionally, the setup of 80 ICs in both the aqueous solution and the vacuum for the PST1, PST2, PST5, PST7, and PST27 follows the procedure outlined in the ref 45.

All ground-state QM/MM MD simulations were performed with the TeraChem[48−51] software package interfaced with the OpenMM[55] package.

AIMS Simulation. For each PST-tubulin system, starting from the 80 ICs prepared in the above-mentioned procedure, the AIMS simulations were initiated by populating each trajectory in the first singlet excited state (S_1 state). The full multiple spawning (FMS) algorithm propagates the nuclear-electronic wave functions represented by trajectory basis functions (TBFs) on multiple electronic states. Each TBF is a multidimensional frozen-width Gaussian nuclear basis function living on a specific electronic state. Its centroid represents the coordinates of all atoms in the entire system. Each TBF is associated with an electronic degree of freedom, i.e., the complex amplitude of the electronic state to which it belongs. Each TBF's centroid travels classically on a specific electronic state to which it belongs. The time-dependent Schrodinger's equation governs the coupled time evolution of the amplitudes of all TBFs propagated on different states, which naturally leads to interstate population transfers. In the FMS algorithm, for most cases, the dominating population transfer events occur during new TBF spawning events. Whenever a TBF on state A visits a region featuring high nonadiabatic coupling with state B (defined by the scalar product between the nonadiabatic coupling vector and the

velocity vector beyond a threshold value), the spawning of new TBFs on state B will be triggered, and the TBF amplitude of state A will be transferred at least partially to the new TBF on state B, resulting in population transfer between these two states. If the spawning event is infrequent, the total number of original and newly spawned TBFs will be small, making their dynamic propagation computationally efficient and accurate. Notably, since the atoms experience different forces and accelerations on different electronic states, the overlap between TBFs on these states typically decreases quickly over time, and the evolution of their state-specific amplitudes naturally decouples, leading to the correct electronic decoherence behavior. This is an important advantage over conventional nonadiabatic methods such as Ehrenfest and surface hopping, which, without decoherence corrections, can lead to an incorrect description of the population transfer dynamics between states. The quantum yield of the photodynamics can be predicted based on the relative amplitudes of ground-state TBFs ending up in the minima corresponding to the photoproducts and reactants. In the AIMS simulations, the energies, forces and nonadiabatic coupling vectors of the TBFs' centroids are calculated on the fly by *ab initio* electronic structure methods. In this study, these quantities were calculated using the hh-TDA-BH&HLYP/6-31G*/MM method in the above-mentioned QM/MM setting.

The three lowest singlet states (S_0, S_1, and S_2) were included in the AIMS simulations. A time step of 20 au was used for the noncoupling region, and 5 au time step was used in the coupling region where spawning events may occur. The propagation continued until over 95% of the S_1 population had relaxed to the ground state.

To characterize the excited-state population decay time constant for each system, the time evolution of S_1 state population $P_{S_1}(t)$ was first analyzed using the AIMS simulations started from all 80 ICs. Then it was fit to a first-order kinetics model (eq 1):

$$P_{S_1}(t) = \exp\left(-\frac{t}{\tau}\right) \tag{1}$$

where t is the time after photoexcitation, and τ is the time constant characterizing excited-state population decay to the ground state.

To evaluate the photoisomerization quantum yield, we calculated the ratio of ground-state TBFs whose centroids ended as the *trans* isomer to the total ground-state population, defining the *trans* isomer as having a final $|\theta_{CNNC}| > 90°$ at the end of the AIMS simulation. Such a criterion was benchmarked to successfully predict the final outcome of extending the post-AIMS adiabatic S_0-state dynamics in the protein environment studied here (for PST1) and in the aqueous solution.[34] To estimate uncertainties of the time constants and quantum yield, bootstrapping over 1000 random samples of the ICs were performed.

Absorption Spectra Calculations. For PST1, PST7, and PST27, snapshots were selected from the final 3 ps of each of the 80 ground-state BH&HLYP/MM MD trajectories at 10 fs time intervals, yielding a total of 24,000 geometries for each PST in both the protein and aqueous solution. Single-point energy calculations were then performed on these geometries using the hh-TDA-BH&HLYP/6-31G*/MM approach with the same QM/MM settings as the AIMS simulations. The excitation energy and oscillator strengths for the $S_0 \rightarrow S_1$

transitions were collected from all calculations, based on which the absorption spectra were calculated following the approach outlined in ref 56. Lorentzian functions with full width at half-maximum (FWHM) of 0.02 eV were used for convolving the discrete data points to generate continuous absorption spectra.

Excited State QM/MM Umbrella Sampling Simulation. The S_1-state free energy surface (or, potential of mean force, PMF) for the PST1, PST7, and PST27 were calculated using QM/MM umbrella sampling (US). We used 10 evenly spaced umbrella windows with centers ranging from $\theta_{CNNC} = 0$ to 90°, incrementally driving the PST's θ_{CNNC} torsion from the *cis* isomer toward the conical intersection seam space. A harmonic restraint with a force constant of 200 kcal/mol/radian^2 was used for restraining the θ_{CNNC} torsion near the center of each window. The QM/MM setting and levels of theory were the same as the AIMS simulations.

The final snapshot from the ground-state QM/MM simulation was used to initialize the first window of the US simulation, with initial structures for other windows subsequently generated by gradually shifting the biasing potential from the previous one. Each window was equilibrated for 1 ps, with the final configuration of one window serving as the starting point for the next. After equilibration, all 10 US windows were run for an additional 4 ps, which were treated as production simulations. The potential of mean force (PMF) was computed using the weighted histogram analysis method (WHAM)[57] to remove bias in the collective variable distribution. Error bars were estimated via block averaging analysis. The PLUMED plugin[57] interfaced with the TeraChem software package[48−51] was used to perform all umbrella sampling simulations.

Benchmark Calculation with XMS-CASPT2 Method. To validate the accuracy of hh-TDA-BH&HLYP/6-31G* method of predicting the ground and excited-state PESs of PSTs, in previous studies[16,34] we extensively benchmarked it against the extended multistate complete active space second-order perturbation theory (XMS-CASPT2) method.[58−61] In addition, previous studies[13,14,16,33,32,62] have demonstrated the reliability of this method in describing the photodynamics of azobenzene and its derivatives. Additional XMS-CASPT2 calculations for the PST7 and PST27 were performed in this study following the same setting (XMS-CASPT2/SA-3-CASSCF(10e,8o)/cc-pVDZ, i.e., (10e,8o) active space, 3-state averaging, 0.2 au imaginary shift, cc-pVDZ basis set) described in our previous studies.[16,34] The active space orbitals are illustrated in Figures S6 and S7. All XMS-CASPT2 optimizations and single-point energy calculations were performed using the BAGEL software package.[63,64]

Thermodynamic Integration (TI). The TI method was employed to quantify the effects of substituents on the binding affinity contrast between *cis* and *trans* isomers of PSTs.

$$\Delta\Delta G_{\text{binding, } cis \text{ PSTX vs. } cis \text{ PST1}}$$
$$= \Delta G_{\text{binding, } cis \text{ PST1}} - \Delta G_{\text{binding, } cis \text{ PSTX}}$$
$$= \Delta G_{cis \text{ PSTX} \rightarrow cis \text{ PST1, bound}} - \Delta G_{cis \text{ PSTX} \rightarrow cis \text{ PST1, unbound}} \tag{2}$$

$$\Delta\Delta G_{\text{binding, } trans \text{ PSTX vs. } trans \text{ PST1}}$$
$$= \Delta G_{\text{binding, } trans \text{ PST1}} - \Delta G_{\text{binding, } trans \text{ PSTX}}$$
$$= \Delta G_{trans \text{ PSTX} \rightarrow trans \text{ PST1, bound}}$$
$$- \Delta G_{trans \text{ PSTX} \rightarrow trans \text{ PST1, unbound}} \tag{3}$$

$$\Delta\Delta\Delta G_{\text{PSTX} \rightarrow \text{PST1, } cis \text{ vs. } trans \text{ binding}}$$
$$= \Delta\Delta G_{\text{PST1, } trans \text{ vs. } cis} - \Delta\Delta G_{\text{PSTX, } trans \text{ vs. } cis}$$
$$= [\Delta G_{\text{binding, } cis \text{ PST1}} - \Delta G_{\text{binding, } trans \text{ PST1}}]$$
$$- [\Delta G_{\text{binding, } cis \text{ PSTX}} - \Delta G_{\text{binding, } trans \text{ PSTX}}]$$
$$= [\Delta G_{\text{binding, } cis \text{ PST1}} - \Delta G_{\text{binding, } cis \text{ PSTX}}]$$
$$- [\Delta G_{\text{binding, } trans \text{ PST1}} - \Delta G_{\text{binding, } trans \text{ PSTX}}]$$
$$= \Delta\Delta G_{\text{binding, } cis \text{ PSTX vs. } cis \text{ PST1}}$$
$$- \Delta\Delta G_{\text{binding, } trans \text{ PSTX vs. } trans \text{ PST1}} \tag{4}$$

Figure 2 illustrates the thermodynamic cycle for the TI simulation, which was constructed to calculate the relative
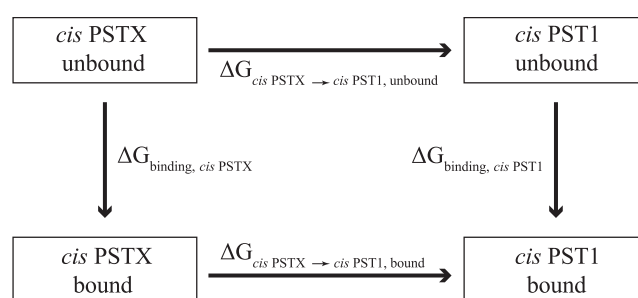
Figure 2. Thermodynamic cycle for calculating the relative binding energies between the *cis* isomers of PST1 and PSTX derivatives (PST4, PST7, and PST27). The horizontal arrows indicate the free energies of alchemical transformation from PSTX to PST1 calculated by the TI simulations in both the aqueous solution (unbound) and protein (bound). The vertical arrows represent the binding free energies of the PSTX and PST1 from aqueous solution to the protein. Analogous thermodynamic cycles were constructed for the trans isomers. The eqs 2−4 detailed the process of calculating the relative binding free energies and the relative *cis*-vs.-*trans* binding free energy contrast between different PSTs.

binding affinity between a pair of PSTs in the same isomer form. For each pair of two PSTs (e.g., *cis* PST1 vs. *cis* PST7), their relative binding affinity was calculated by two sets of TI simulations that predict the free energy change for the alchemical transformation from one compound to the other: one in the aqueous solution (e.g., $\Delta G_{cis \text{ PST7} \rightarrow cis \text{ PST1, unbound}}$) and the other in the protein environment (e.g., $\Delta G_{cis \text{ PST7} \rightarrow cis \text{ PST1, bound}}$). The relative binding affinity between these two compounds in the same isomer form can be calculated (e.g., $\Delta\Delta G_{\text{binding, } cis \text{ PSTX7 vs. } cis \text{ PST1}}$) following eqs 2 and 3, which can be directly compared to the experimental binding affinity difference estimated based on their EC_{50} values (see below).

The relative binding affinities between all PSTX-vs.-PST1 pairs were estimated (with "PSTX" being PST4, PST7, or PST27) in both the *cis* and *trans* isomer forms. Then, the substituents' effect on the *cis*-vs.-*trans* binding affinity contrast
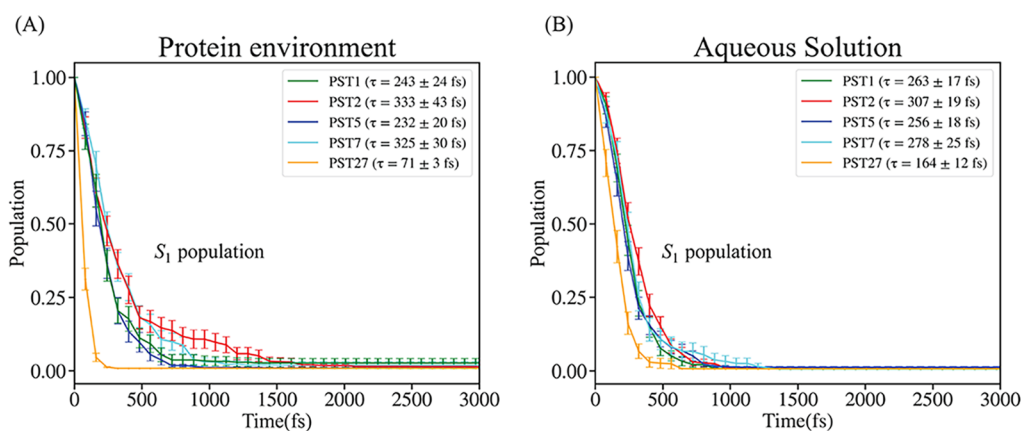
Figure 3. Time evolution of S_1-state population during *cis*-to-*trans* photoisomerization of PST1 (green), PST2 (red), PST5 (blue), PST7 (cyan), and PST27 (orange) in the (A) tubulin protein environment and (B) aqueous solution. The time constants of the S_1 state population decay are reported in the legends.

were estimated using eq 4. For example, $\Delta\Delta\Delta G_{PST7\rightarrow PST1,\ cis\ vs.\ trans\ binding}$ indicates the change in the *cis*-vs.-*trans* binding affinity contrast upon changing PST7 to PST1. A positive $\Delta\Delta\Delta G$ value indicates higher *cis*-vs.-*trans* binding affinity contrast in PSTX than PST1. In other words, photoswitching the *trans* to *cis* isomer induces a higher enhancement in the binding affinity of PSTX than PST1, and PSTX exhibits more light-responsiveness in its binding affinity.

To prepare the TI simulations, the systems were set up and equilibrated by MD simulations in the constant NPT ensemble following the protocol described above, with the exceptions that the TIP3P water model and the SHAKE algorithm was employed to constrain all covalent bonds involving hydrogen atoms, allowing for an integration time step of 2 fs.

A dual-topology approach was employed for the TI simulations transforming PSTX to PST1. All the atoms that differ between the two PSTs underwent a three-stage alchemical transformation process. First, the partial charges on all disappearing atoms in PSTX are gradually scaled down from 100% to zero. Second, the van der Waals and covalent bonds terms associated with the disappearing atoms in PSTX were gradually scaled down to zero, while these force field terms in the appearing atoms in PST1 were gradually scaled up to 100%, keeping their partial charges at zero. Finally, the charges of appearing atoms of PST1 were gradually scaled up to 100%. In each of the three stages, 11 intermediate windows were employed with a 0.1 spacing of the order parameter lambda (λ) mixing the two Hamiltonians associated with the two PSTs. At least 10 ns simulation was performed for each of the systems per windows based on the convergence of the final result. The statistical uncertainty of the free energy changes was estimated by block average analysis.

Molecular Mechanics Poisson–Boltzmann Surface Area (MM/PBSA) Simulations. To assess the performance of end-point free energy methods for predicting the *cis*-vs.-*trans* binding affinities contrasts of the PST and the tubulin, we analyzed the final 100 ns of the production MD trajectory using the MM/PBSA approach. In the calculations, a dielectric constant of 80 was assigned to the solvent while a dielectric constant of 4 was used for the protein to reflect its lower polarizability. A solvent probe radius of 1.4 Å was applied to model the solvent-accessible surface area, and standard force field parameters were used to define the atomic radii of the system components. This setup ensures consistency with

commonly accepted protocols for MM-PBSA calculations in biomolecular simulations.[65,66]

Estimation of Relative Binding Free Energies from Experiments. The EC_{50} values of the PST derivatives investigated here were measured experimentally from cancer cell viability data.[8,24,27] Here we assume that they are linearly correlated with the inhibition constant K_i (or approximately the dissociation constant K_d) of the PST derivatives.

The experimental binding free energy difference between a pair of compounds A and B was thus calculated with eq 5:

$$\Delta\Delta G_{binding,\ A\ vs.\ B}(experiment) = RT\ln\left(\frac{EC_{50}(B)}{EC_{50}(A)}\right) \tag{5}$$

where R is the ideal gas constant, T is the temperature (300 K). The identities of A and B can be defined in two scenarios. In the first, they are the same compound in different isomer forms, e.g., *cis* PST1 vs. *trans* PST1, where the $\Delta\Delta G_{binding,\ A\ vs.\ B}$ represents the binding affinity difference between the *cis* and *trans* isomers. Alternatively, they can be different compounds in the same isomer forms, e.g., *cis* PST1 vs. *cis* PST7, where the $\Delta\Delta G_{binding,\ A\ vs.\ B}$ indicates the relative binding affinity between the two compounds in the *cis* isomer. In either scenario, the quantity $\Delta\Delta\Delta G_{PSTX\rightarrow PST1,\ cis\ vs.\ trans\ binding}$ can be estimated using eq 4 based on the $\Delta\Delta G_{binding,\ A\ vs.\ B}$.

■ RESULT

One of our primary goals is to elucidate how the substituents and environmental embedding affect the excited state isomerization dynamics in a class of photoswitchable ligands named PST derivatives (Figure 1). To this end, we employed AIMS simulations coupled with excited-state electronic structure calculations to characterize the kinetics and quantum yields of a representative set of five azobenzene-based photoswitches, namely PST1, PST2, PST5, PST7, and PST27, in the tubulin dimer and aqueous solution. To mechanistically analyze these systems, we examined the effects of substituents and molecular environment through a multifaceted analysis of energetics and dynamics. This is achieved by characterizing the excited-state free energy and potential energy surfaces (PESs), absorption spectra, electrostatic environment, steric restrictions, and nonradiative decay dynamics to reveal how substituents and environment modulate photoisomerization. Then, we benchmarked different free energy methods for quantifying the

substituent-dependent binding free energy differences between distinct isomeric states in a complex protein environment. Finally, we discuss the details of the methods we employed in the spectra calculation and nonadiabatic dynamics simulations.

Kinetics and Quantum Yields of Photoisomerization. From AIMS simulations, we extracted the time evolution of S_1-state population following the S_0 to S_1 $n\pi^*$ photoexcitation of PST1, PST2, PST5, PST7, and PST27 embedded in the interface of the tubulin dimer (Figure 3A) and solvated in aqueous solution (Figure 3B). The decay of the S_1-state population accompanies the *cis*-to-*trans* photoisomerization, and the time constants of this process (Figure 3A,B) were estimated using first-order decay kinetics (Method). We also analyzed the structures of the centroids of ground-state trajectory basis functions (TBFs) and their amplitudes to calculate the photoisomerization quantum yields (Table 1).

Table 1. Calculated *Cis*-to-*Trans* Photoisomerization Quantum Yields of PST1, PST2, PST5, PST7, and PST27 in Protein Environment, Aqueous Solution, and the Vacuum[a]

Molecule	Protein environment	Aqueous solution	Vacuum
PST1	47 ± 5%	45 ± 4%*	48 ± 4%*
PST2	55 ± 4%	43 ± 4%*	50 ± 5%*
PST5	56 ± 5%	43 ± 4%*	46 ± 4%*
PST7	53 ± 5%	49 ± 5%	49 ± 4%
PST27	43 ± 5%	40 ± 4%	41 ± 5%

[a]Data from ref 34. Some of the data (labeled with *) are reproduced with permission from ref 34. Copyright 2025 John Wiley and Sons.

For each compound in each environment, the kinetics and quantum yield were averaged over 80 initial conditions (ICs) sampled by ground-state QM/MM simulations (see Method for details) in the *cis* isomers' Franck−Condon region.

The data in Table 1 demonstrate that both the substituents and the molecular environment substantially influence the quantum yields (QYs) of the PST derivatives. The substituents have a major effect on the QYs in both environments. In the protein environment, PST27 has the lowest quantum yield (QY) of 43 ± 5%, whereas PST5 has the highest QY of 56 ± 5%, differing by as much as 13%, which exceeds the statistical uncertainty. In the aqueous solution, PST27 has the lowest QY of 40 ± 4%, whereas PST7 has the highest QY of 49 ± 5%, differing by 9%. Regarding the effects of the environment, all PSTs increase their QYs when transitioning from an aqueous

solution to a protein environment. The PST2 and PST5 exhibit the highest increases, i.e., 12 and 13%, accounting for ~28 and ~30% increase relative to the QYs calculated aqueous solution, respectively. Consequently, the trends of QYs of PSTs differ in different environments. In the aqueous environment, the order is PST7 > PST1 > PST5 ≈ PST2 > PST27. In the protein environment, the order is altered: PST5 ≈ PST2 > PST7 > PST1 > PST27. This reordering is mainly due to the protein environment having different enhancement effects on the QYs of different PSTs. Notably, for PST1, the QY in the protein environment agrees reasonably well with a recent study[21] employing ultrafast time-resolved crystallography and spectroscopy to investigate the photodynamics of the same system, which reported a QY of ~40 ± 10%. The relaxation time constant is also consistent with experimental data (150−250 fs).[21] The agreement with ultrafast time-resolved experiment confirms the accuracy of our nonadiabatic dynamics simulation method.

Substituents also have a major effect on the time constants of the S_1-state population decay (Figure 3). For example, PST27 and PST2 exhibit the shortest and longest relaxation time constants among all PSTs in both environments, respectively. Their time constants differ by as much as 262 ± 43 fs in the protein and 143 ± 22 in aqueous solution, much beyond their statistical uncertainties. The effect of protein, however, does not exhibit a clear trend among the PSTs. Shifting from the aqueous solution to the protein environment decreases the S_1-state lifetime of PST27 (from 164 ± 12 to 71 ± 3 fs), but increases that of PST7 (from 278 ± 25 to 325 ± 30 fs). For other PSTs, the change in the S_1-state lifetime is not significant compared to statistical uncertainty.

From the perspectives of energetics and dynamics, we interpret the effects of substituents and environment on the kinetics and quantum yields of the PSTs below.

S_1-State Free Energy Surface. To understand what affects the kinetics of the photoisomerization, we calculated the QM/MM potential of mean force (PMF, i.e., the free energy surface) on the S_1 state corresponding to the excited-state isomerization process in the protein and aqueous solution. The PMFs were calculated as a function of the θ_{CNNC} torsion around the central N═N double bond using umbrella sampling (US) simulations, which covered the range from the FC region (~0°) to the MECI (~90°) in a series of biased simulations. The excited-state US simulations were performed
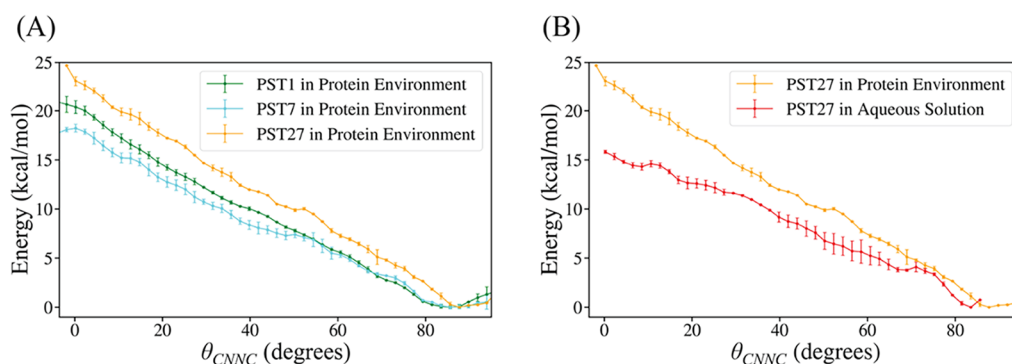
Figure 4. Free energy profiles along the central θ_{CNNC} dihedral on the S_1 excited state from the *cis* isomer's Franck−Condon region ($\theta_{CNNC} \sim 0°$) to the conical intersection seam ($\theta_{CNNC} \sim 90°$). (A) The effects of substituents on the free energy profile in the protein environment, comparing PST1 (green), PST7 (cyan), and PST27 (yellow). (B) The effects of molecular environment on the free energy profiles of PST27, comparing the protein (yellow) and aqueous solution (red).

in the same QM/MM setting as the AIMS simulation (see Method for details). The PMFs of PST1, PST7, and PST27 in the protein environment (Figure 4A) were compared in order to elucidate the substituents' effects. These three PSTs were selected due to their representative S_1-state decay time constants: the PST27 and PST7 have one of the shortest and longest time constants, respectively, and the time constant of PST1 is in the middle range (Figure 3A). Also, the comparison between PST1 and PST7 is highly interesting because they only differ by one methylene (CH_2) group in the R_3 substituent on Ring A (Figure 1B). Additionally, we compared the PMFs of PST27 in aqueous solution versus protein environment (Figure 4B) to understand the effects of protein environment on the photoisomerization kinetics. This compound was selected because the protein environment significantly accelerates the kinetics of the photoreaction, making it an important case to study the protein's catalytic effect on photochemical reactions of synthetic, non-native photoswitches (Figure 3A,B).

The results in Figures 4 and S1 illustrate that the S_1-state population decay time constants are inversely correlated with the overall slopes of the corresponding PMF curves. For example, the PMF of PST27 in protein has a much larger slope than in the aqueous solution, leading to faster S_1-state population decay. In the protein environment, the trend of the slopes follows the order PST27 > PST1 > PST7, which is inversely correlated with their trend in time constants, i.e., PST7 > PST1 > PST27. Thus, this free energy calculation and analysis reveal a simple but fundamental physical picture of photoisomerization kinetics: a larger free energy slope leading from the FC region to the MECI region leads to a quicker rotation around the N=N double bond, which facilitates the decay of the S_1-state population. Such a correlation is evident in Figure S1. This analysis is significant in that it validates a solid connection between the nonequilibrium, multistate nonadiabatic photodynamics with the equilibrium free energy surface on a single excited state (S_1 state). Such a connection can only be rigorously verified through explicitly sampling conformational fluctuations and propagating the nonadiabatic photodynamics, as was done in this study.

The effect of substituents, particularly electron-donating groups such as methoxy groups, on the S_1-state relax-scanned PES was investigated by comparing PST1 and PST27 (Figure S9). The PST27 has three fewer methoxy groups than the PST1, which were replaced by alkyl groups (Figure 1). The PST1 exhibits a smaller FC-to-MECI energy gap and a smaller slope in the PES than PST27. In qualitative terms, the electron-donating substituents (e.g., methoxy) increase the relative stability of the FC with respect to the MECI, reducing the driving force toward the CI. This trend is consistent with our S_1-state PMFs (Figure 4).

Absorption Spectra and Excitation Energies. To further understand how substituents and the protein environment affect the energetics of the S_1 state, we calculated the absorption spectra based on the conformations sampled from ground-state QM/MM MD simulations for the PST1 and PST27 (Method) contributed by the S_0 to S_1 excitations.

Different substituents and molecular environments result in distinct absorption peaks (Figure 5). Using the *cis* PST1 as the reference, in the protein environment, PST27 exhibits a 0.16 eV blue shift in the maximum absorption. However, in the aqueous environment, PST27 is blue-shifted by only 0.078 eV from PST1, which agrees reasonably well with previous
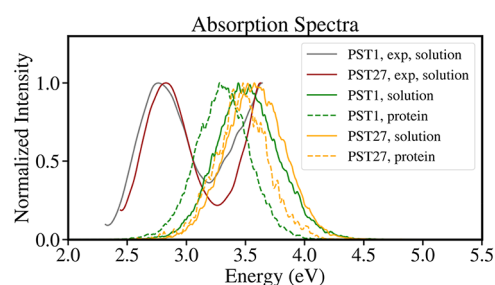

Figure 5. Calculated absorption spectra contributed by the $S_0 \rightarrow S_1$ photoexcitation of the *cis* isomers for PST1 and PST27 in the tubulin and aqueous solution. For each PST, solid and dashed lines indicate absorption spectra in aqueous solution and protein, respectively. The solid gray and red lines represent the experimental spectra of PST1 (ref 8) and PST27 (ref 27) in solutions.

experiments (~0.03 eV).[8,24,27] The observed spectral shifts are consistent with the S_0-S_1 energy gap in the gas phase at the *cis* isomer minima as predicted by both the hh-TDA-BH&HLYP and XMS-CASPT2 levels of theory (Table S1). The results reveal the order of S_0-S_1 energy gaps as PST1 < PST27, which is consistent with the blue-shifts observed in the absorption spectra for PST27 relative to PST1 (Figure 5). Interestingly, the PST27 blue-shifts the spectra because it replaces the three methoxy groups ($-OCH_3$) on both rings A & B (R_1, R_2, and R_3) of PST1, which are strong electron-donating group, with three alkyl groups (two ethyl and one methyl groups, see Figure 1B).

Importantly, the protein environment red-shifts absorption spectra for all three compounds relative to the aqueous solution. The shifts are in the range of ~0.1−0.2 eV. The experimental absorption spectrum of PST1 contributed by the S_0 to S_1 excitation was measured in the presence of MeCN cosolvent (Figure 5).[8] Compared to the experiment, the PST1's spectrum calculated by the hh-TDA-BH&HLYP/MM method has an overall blueshift of ~0.7 eV, possibly due to the difference in the solvent, the partitioning between QM and MM regions, and the lack of polarization in the MM atoms' point charges. Although the absolute wavelength of maximum absorption was not predicted with high accuracy, the relative trend of spectral shifts among the calculated spectra provides new insights into how the substituents and protein environment affect the photophysical properties of the PSTs.

Effects of Protein Electrostatics. In order to probe the effect of protein electrostatics on the kinetics of S_1-state population decay, for each PST, we analyzed the type of MECI mediating the majority of the $S_1 \rightarrow S_0$ population decay (>50%), and optimize its structure within the protein environment (for more details, see Figure 6 and below) at hh-TDA-BH&HLYP/MM level of theory. Following this, the FC point corresponding to the *cis* isomer minimum on the ground state was also optimized at BH&HLYP/MM level of theory (consistent with the ground-state QM/MM equilibration), while constraining the MM atoms beyond 5 Å of the PST. The energy difference between the FC point and the MECI on the S_1 state, i.e., $\Delta E = E(S_1, FC) - E(S_1/S_0, MECI)$, was calculated for each PST at the hh-TDA-BH&HLYP/MM level of theory on top of these two geometries. Each ΔE calculation was performed twice: first time with full point charges of the MM region, i.e., the protein, cofactor and solvent molecules, and the second time with all MM point charges artificially set to zero. The results are summarized in
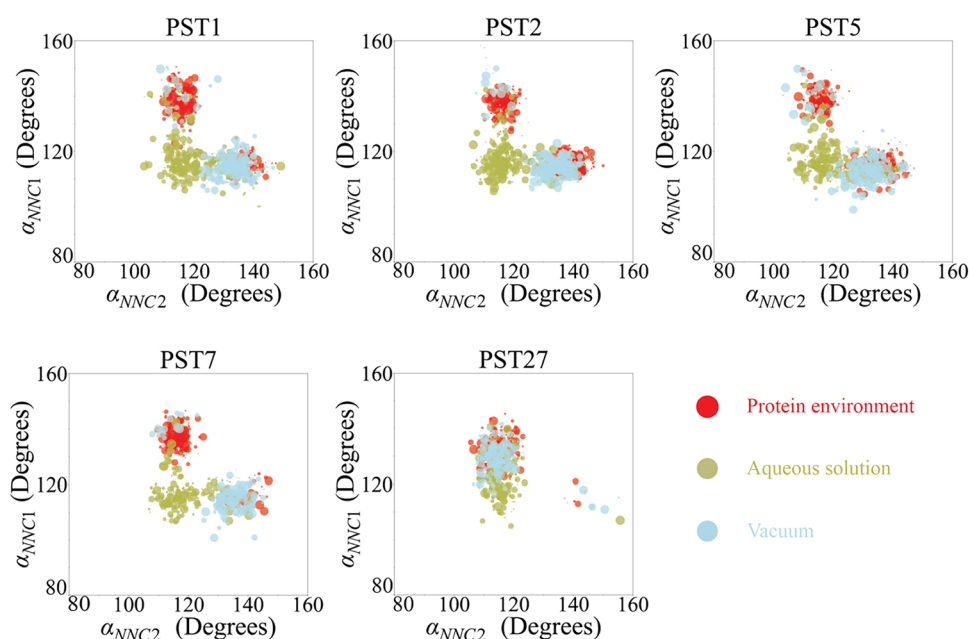
Figure 6. Geometries of the ground-state TBF centroids at the $S_1 \rightarrow S_0$ spawning time points projected onto the 2D planes spanned by the α_{NNC2} and α_{NNC1}. The radius of the circle around each projected geometry is proportional to the eventual population of the S_0 TBF. Data points in the protein environment, the aqueous solution, and the vacuum are shown in red, green, and cyan colors, respectively.

Table 2. The difference in these two ΔE's qualitatively reflects the impact of protein and solvent electrostatics on the slope of

Table 2. Difference in the S_1-State Potential Energy (in kcal/mol) between the *Cis* Isomer's Franck-Condon (FC) Region and the S_1/S_0 MECI Optimized in the Tubulin Protein Environment, i.e., $\Delta E = E(S_1, FC) - E(S_1/S_0, MECI)$[a]

System	ΔE (full MM charge)	ΔE (zero MM charge)	Relaxation time in tubulin	Relaxation time in the vacuum
PST1	30.46	25.50	243 ± 24	154 ± 8*
PST2	27.36	22.95	333 ± 43	167 ± 10*
PST5	29.82	24.11	232 ± 20	111 ± 8*
PST7	27.85	26.23	325 ± 30	165 ± 13
PST27	36.22	33.28	71 ± 3	88 ± 5

[a]Data from ref 34. The ΔE's were calculated at the hh-TDA-BH&HLYP/MM level of theory with full and zero MM point charges. The relaxation time constants (in fs) of the S_1 state in the protein and vacuum are also summarized. Some of the data (labeled with *) are reproduced with permission from ref 34. Copyright 2025 John Wiley and Sons.

the S_1 state PES from the *cis* isomer to the MECI, which was shown to be inversely correlated with the S_1-state relaxation time in the vacuum.[34] Here, such a correlation is also evident in the protein environment (Figure S2).

The data in Table 2 indicate that protein electrostatic environment in general increases the energy gap between the FC region and the MECI, and can in principle facilitate the photoisomerization on the excited state. However, comparing the relaxation time constants in both protein and vacuum environments, the protein usually has slower population decay, except for PST27. This indicates that steric effects in the protein may also reshape the dynamics of the excited-state photoisomerization, which are analyzed below.

To assess whether the S_1 decay involves significant charge transfer (CT), we monitored the change in the total S_1-state Mulliken charge on either of the two benzyl rings A and B, along the relaxed-scanned PES from the FC to the MECI on the S_1 state in the vacuum (Figure S9, eq 6):

$$\Delta q_A^{path}(w) = q_A^{S_1}(w) - q_A^{S_1}(FC)$$

$$\Delta q_B^{path}(w) = q_B^{S_1}(w) - q_B^{S_1}(FC) \tag{6}$$

where the $\Delta q_A^{path}(w)$ and $\Delta q_B^{path}(w)$ are the changes in the S_1-state total charge compared to the FC point on the ring A and B (Figure 1), respectively, and w is a reaction coordinate describing the photoisomerization, selected to be the θ_{CNNC}.

For PST1, the maximum changes in the charges are small: $|\Delta q_A^{path}| = 0.0439$ e and $|\Delta q_B^{path}| = 0.0177$ e. Meanwhile, the charges on the azo group's two nitrogen atoms change by at most 0.0810 and 0.0461 e. For PST27, the CT remains similarly modest: changes in charges of the nitrogen atoms are at most ~0.059 and 0.063 e, and at most ~0.043 e and ~0.042 e for the ring A and B, respectively. The small magnitudes in the Δq's indicate no substantial intramolecular CT along the S_1-state pathway in either system.

Additionally, we investigated the electrostatic effect from each individual residue near the PST. This was done by zeroing out only the MM point charges of a single residue, and recomputing the S_1-state energy of the system using hh-TDA-BH&HLYP/MM method at the FC and MECI, without further geometric relaxation. Removing all MM atoms' charges significantly decreases the FC to MECI energy gap. When removing MM charges from individual residues, charged and polar residues exhibit a larger effect on the energy gap than the hydrophobic ones. Zeroing out the charges on the Asp700 and Lys801 residues results in the largest energy gap reductions, whereas nearby neutrals led to much smaller changes (Table S2). These results indicate that the contribution to the

increased energy gap between FC to MECI is most likely due to the presence of these charged and polar residues.

Steric Restrictions. Steric restrictions imposed by the ligand-binding pocket in the protein can hinder intramolecular motions associated with isomerization, potentially prolonging the relaxation time. To quantify the steric effects, following ref 14, we computed the average and variance of the contact number (N) of ligand atoms using all AIMS TBFs on the S_1 state that have successfully decayed to the S_0 state. The contact number corresponds to the number of atoms in the protein and water molecules that are located within 2−3 Å of the PST molecule, which is defined in eq 7:

$$N = \sum_{i \in \text{PST}} \sum_{j \in \text{Env}} \frac{1 - \left(\frac{r_{ij} - d_0}{r_0}\right)^6}{1 - \left(\frac{r_{ij} - d_0}{r_0}\right)^{12}} \tag{7}$$

where r_{ij} is the pairwise distance between atom i in the PST and atom j in the surrounding environment. Parameters $d_0 = 2.5$ Å and $r_0 = 0.5$ Å were selected to define the center and thickness of the contact shell between the PST and the environment. The variance of the contact number N ($\overline{\sigma_N^2}$) is correlated with the reversible work needed to push the atoms in the surrounding environment away from the ligand during its photoisomerization,[67] with smaller variance corresponding to a more rigid and stronger kinetic caging effect.[14]

Table 3. Average ($\bar{N}$) and Variance ($\overline{\sigma_N^2}$) of the PSTs' Contact Number N for the S_1-State Dynamics of the PSTs in the Protein Environment and Aqueous Solution[a]

Molecule	Quantity	Protein environment	Aqueous solution
PST1	$\bar{N}$	105.70	122.83
	$\overline{\sigma_N^2}$	35.71	80.73
PST2	$\bar{N}$	112.28	127.07
	$\overline{\sigma_N^2}$	44.77	69.85
PST5	$\bar{N}$	89.12	112.60
	$\overline{\sigma_N^2}$	32.83	67.24
PST7	$\bar{N}$	115.64	125.87
	$\overline{\sigma_N^2}$	48.68	77.98
PST27	$\bar{N}$	100.76	115.26
	$\overline{\sigma_N^2}$	24.38	58.89

[a]For each PST, the data is averaged over all S_1-state TBFs launched from all ICs before the first $S_1 \to S_0$ spawning event.

As shown in Table 3, for all PSTs' S_1-state dynamics, the $\overline{\sigma_N^2}$ in the protein environment is consistently lower than the aqueous solution. This indicates that the residues impose a more rigid scaffold surrounding the PSTs, leading to stronger caging effect than the water molecules in the bulk solution. Compared with the vacuum, which has no atoms in the surrounding environment, the kinetic caging effect of protein is expected to be even more pronounced. Thus, the slower excited-state photoisomerization dynamics in the protein compared with the vacuum is largely due to the stronger steric restrictions and caging effects. The aqueous solution already imposes noticeable steric confinement (variance ~60−

80) compared to the vacuum, which slows excited-state isomerization.[34] In the protein, the variance drops to ~25−50, indicating a more rigid scaffold from the environment and stronger kinetic caging. Thus, this quantitative analysis directly compares the steric effects in the vacuum, aqueous solution, and protein, elucidating how it modulates the excited-state decay kinetics.

The steric restrictions imposed by the protein also modify the ground-state conformational distribution of the PSTs (Figure S3), which affects the photodynamics. Across all systems in protein environment, the ICs of the *cis* isomer PSTs have positive θ_{CNNC} torsions, and the PSTs all decay through the MECI with ~90° θ_{CNNC} torsion (Figures S4 and S5). This is in sharp contrast to PST photodynamics in the vacuum and aqueous solution, featuring both positive and negative θ_{CNNC} torsions in the ICs and bidirectional photoisomerization accessing MECIs with both ~90 and ~−90° θ_{CNNC} torsions (Figures S4 and S5, and ref 34). The protein's influence on the directionality of the photoisomerization is another manifestation of the steric restrictions. Due to the steric restrictions biasing the PSTs toward the more positive values compared to the aqueous solution and gas phase, the PSTs have a slight head start in the excited-state photoisomerization process, which may facilitate the nonradiative decay in the protein environment. In particular, hydrogen bonding and steric constraints from surrounding residues in close contact with the PST ligand can potentially modulate its conformational flexibility and excited-state decay dynamics. Although our simulations do not quantitatively isolate the contributions of each individual residue, their spatial proximity to the ligand suggests a plausible role in shaping the relaxation dynamics during photoisomerization. It is worth noting that mutation of residues near the chromophore, such as Val313→Phe313, could increase steric hindrance and potentially slow down the dynamics by restricting torsional motion. Similarly, an Asn256→Ala256 mutation may alter local polarity and H-bonding, potentially modulating the kinetics of the photo-isomerization.

Nonradiative Decay Channels. To understand how the substituents and molecular environments affect the non-adiabatic transition events, we analyzed the geometries at which the $S_1 \to S_0$ spawning events occurred during the AIMS simulations (Figure 6 and Figures S4 and S5). These spawning geometries are projected to 2D planes spanned by pairwise combinations of three reaction coordinates: θ_{CNNC} (central torsion around N═N bond), α_{NNC1} (N═N−C1 bending angle), α_{NNC2} (N═N−C2 bending angle) (defined in Figure 1B). Each point on the 2D plane corresponds to a geometry at the beginning of the spawning event, with its radius representing the final population of the spawned S_0 TBF at the end of the AIMS simulation. Their geometries represent the main types of MECIs through which the nonradiative decay events occur. These three coordinates had been successfully used to compare the nonadiabatic relaxation channels between the vacuum and aqueous solution in our previous studies.[14,33,34]

It is evident that the protein environment shifts the distribution of the α_{NNC1} and α_{NNC2} angles from the aqueous environment (Figure 6). In the aqueous environment, the distribution has a single peak at (~120°, ~120°). In the protein, however, there are two distinct peaks at (~140°, ~120°) and (~120°, ~140°), analogous to the distributions in the vacuum.[34] In our previous study,[34] we discovered that the
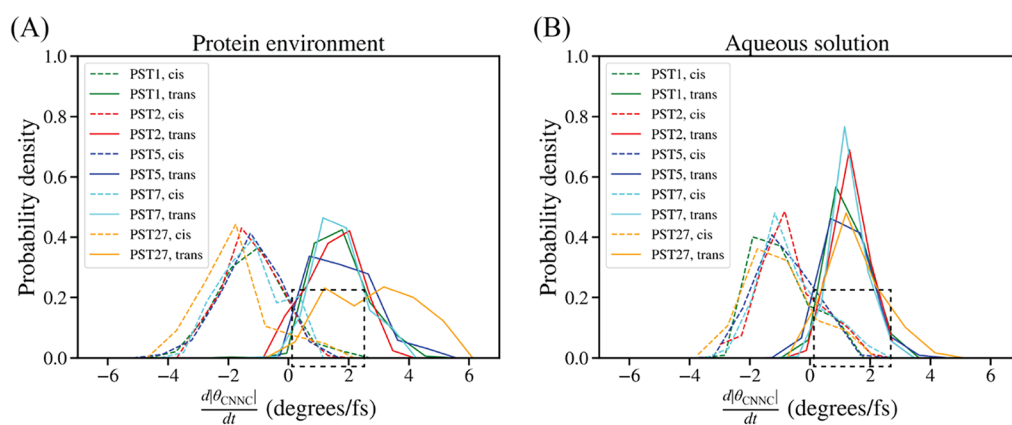
Figure 7. Probability distribution of the velocity of the absolute value of the θ_{CNNC} torsions of the ground-state TBFs at their spawning time points in the (A) protein environment and (B) aqueous solution. The probability is weighted by the final population of each TBF at the end of the AIMS simulation, and categorized by the eventual isomer form of the TBFs (solid lines: *trans* isomer, dashed lines: *cis* isomer). The dashed black boxes highlight the probability distribution contributed by ground-state TBFs, which initially had positive velocity at the spawning time point but eventually ended in the *cis* isomer reactant minimum. Their total populations are summarized in Table 4.

shift from the vacuum to the aqueous solution increases the dielectric constant, which reshapes the topography of the conical intersection seam. The two MECIs in the vacuum sharing the same θ_{CNNC} torsion and having different patterns of asymmetric α_{NNC1} and α_{NNC2} bending angles are merged into one MECI where the two bending angles are similar.[34] Here, a phenomenon similar to the vacuum is observed in the protein. The relatively low dielectric environment in the protein, as characterized by the smaller magnitudes of electric field at PST (Tables S3 and S4), resembles the vacuum environment. Thus, the PSTs retain the two distinct MECIs with different asymmetric bending angles. However, the major difference between protein and the vacuum is that only the MECIs with a θ_{CNNC} torsion at ~90° in the former are observed (Figures S4 and S5), consistent with the unidirectional photoisomerization, whereas in the vacuum the photoisomerization leads to MECIs with a θ_{CNNC} torsion at ~90° and ~−90°, corresponding to bidirectional photoisomerization. Thus, the protein confinement limits the types of nonadiabatic relaxation channels compared to the vacuum.

Additionally, the PST27 exhibits distinct joint distributions of the α_{NNC1} and α_{NNC2} angles at the time of $S_1 \rightarrow S_0$ spawning compared to other PSTs. Notably, PST27 shows more asymmetric joint distributions of α_{NNC1} and α_{NNC2} angles in the protein environment and the vacuum compared to other PSTs, favoring the access to only one type of MECI. This suggests that substituent modifications in PST27 introduce geometric asymmetry that reshapes the excited-state PES, biasing the photodynamics such that only one of four major types of S_0/S_1 MECIs in a typical azobenzene photoswitch[34] is accessed. Consequently, this structural imbalance may lead to faster excited-state population decay, consistent with its short relaxation time (71 ± 3 fs).

Relation between the Torsional Dynamics and Quantum Yield. Our analysis also reveals that the substituents and protein environment perturb the dynamics of θ_{CNNC} at the nonadiabatic transition time, affecting the QY. Figure 7 illustrates the probability distributions of the velocity of the absolute value of the θ_{CNNC} torsion at the spawning time of the S_0 TBFs. The distribution is categorized by the final geometry of the S_0 TBFs' centroids at the end of the AIMS simulation, being either the *cis* or *trans* isomer, and weighted

by the final amplitudes of these TBFs. Comparing the velocity distributions corresponding to the *cis* isomer S_0 TBFs in Figure 7A,B, there is a clear trend that the protein environment reduces the backward flow to the *cis* isomer on the ground state, as evidenced by the less total population above 0°/fs for these back-isomerizing TBFs in the protein environment (Table 4). Also, the protein environment increases the

Table 4. Total Population of S_0-State TBFs with Initial Positive Torsional Velocity at the Spawning Time Point but Eventually Underwent Backward Isomerization and Ended Up in the *Cis* Isomer Reactant Minimum[a]

Molecule	Aqueous solution (%)	Protein environment (%)
PST1	6	3
PST2	9	2
PST5	7	2
PST7	12	7
PST27	4	2

[a]See Figure 7 for definition.

probability of observing torsional velocities with more positive values for the *trans* isomer TBFs (beyond 3°/fs). Thus, the protein environment increases the quantum yield by enlarging the magnitudes of the torsional velocity toward the positive value while reducing the ground-state backward flow that reverses and aborts the isomerization process.

However, comparing different PSTs in the same environment, more positive torsional velocities do not necessarily lead to higher QYs, since the population spawning is also related to the nonadiabatic coupling vector. In PST27, the torsional velocity distribution is more positively shifted compared to other PSTs at the spawning time points of *trans* isomer S_0 TBFs, but its quantum yield is lowest among all PSTs in all three environments (protein, aqueous solution, and vacuum, Table 1).

This is an interesting observation, offering unique insights into the dynamics of population transfer during the state-crossing. The S_0-state population growth accompanying the torsional dynamics toward the positive direction is determined by two factors. The first is the dot product between the all atoms' velocity and nonadiabatic coupling vectors

$\Lambda_{IJ}(\overline{\mathbf{R}}_i) = |\dot{\overline{\mathbf{R}}}_i \bullet \mathbf{d}_{IJ}(\overline{\mathbf{R}}_i)|$, where $\mathbf{d}_{IJ}(\overline{\mathbf{R}}_i)$ and $\dot{\overline{\mathbf{R}}}_i$ are the nonadiabatic coupling vector and velocity vector of all coordinates. This scalar product $\Lambda_{IJ}(\overline{\mathbf{R}}_i)$ dictates the rate of population transfer between states I and J in the FMS[30] algorithm. The second factor is the time duration of the spawning event where significant population transfer occurs. Large positive torsional velocity at the first spawning event may become counterproductive for the QY, since it can reduce the duration of the spawning event and misalign with the nonadiabatic coupling vector, thereby limiting the magnitude of *trans* isomer S_0 TBFs spawned during the initial spawning events. Subsequent excited-state dynamics can lead to passage near the CI seam with negative torsional velocity that better aligns with the nonadiabatic coupling vector, leading to significant population accumulation for the *cis* isomer TBFs. In other words, faster forward isomerization dynamics may totally or partially miss the strong S_0/S_1 coupling region, reducing population accumulation in the first-generation S_0 TBFs ending up in the *trans* isomer minimum, reducing the QY.

Our hypothesis is confirmed and quantified by calculating the conditional QYs, defined as the QYs among only the first and second S_0-state TBFs spawned onto the ground state (Table S5). The conditional QYs characterize the branching ratio of population transfer during the early stage of nonradiative decay events as simulated in the AIMS algorithm. The results illustrate an interesting, consistent trend (Table S5). The conditional QY of PST27 is lower than the other PSTs, while those for PST2 and PST5 are the largest among all PSTs. This analysis confirms our interpretation above, highlighting the importance of directional alignment of the nonadiabatic coupling vector with torsional velocity in increasing the final QYs. This finding also reveals the nontrivial relation between the kinetics and QY of photoisomerization in general.

Substituents' Effects on the *Cis*-vs.-*Trans* Binding Affinity. To assess how chemical modifications affect both the overall binding affinity and the difference between cis and trans binding affinities of the PSTs, we built thermodynamic cycles (e.g., Figure 2) and applied thermodynamic integration (TI) to compute relative binding free energies ($\Delta\Delta G_{binding}$) between PST7 and PST1, PST27 and PST1, and PST4 and PST1 in their *cis* and *trans* forms (eqs 2 and 3). For example, $\Delta\Delta G_{binding,cis\ PSTX\ vs.\ cis\ PST1}$ is defined as the change in binding free energy when converting *cis* PSTX (where X = 4, 7, or 27) into *cis* PST1. A positive $\Delta\Delta G_{binding}$ indicates that PST1 binds less strongly than PSTX.

Using these relative binding free energies for each isomer (i.e., $\Delta\Delta G_{binding,cis\ PSTX\ vs.\ cis\ PST1}$ and $\Delta\Delta G_{binding,trans\ PSTX\ vs.\ trans\ PST1}$), we then calculated the change in the *cis*-vs.-*trans* binding-affinity contrast upon converting PSTX to PST1, i.e., $\Delta\Delta\Delta G_{PSTX\rightarrow PST1,cis\ vs.\ trans\ binding}$ (eq 4). Analogous to the importance of predicting $\Delta\Delta G_{binding}$ in conventional computer-aided drug design, accurately predicting the triple-delta term ($\Delta\Delta\Delta G_{cis\ vs.\ trans\ binding}$) is crucial for designing photoswitchable drugs that maximize light-responsive changes in bioactivity.

Table S6 lists the computed free energy changes for each alchemical transformation between cis or trans PSTX and cis or trans PST1, both in solution (e.g., $\Delta G_{cis\ PSTX\rightarrow cis\ PST1,unbound}$) and in the protein environment (e.g., $\Delta G_{cis\ PSTX\rightarrow cis\ PST1,bound}$). We used these ΔG values to derive the $\Delta\Delta G_{binding}$ and $\Delta\Delta\Delta G$

quantities, which are then directly comparable to the experiment.

To validate our approach, we benchmarked the calculated $\Delta\Delta G_{binding,cis\ PSTX\ vs.\ cis\ PST1}$ and $\Delta\Delta G_{binding,\ trans\ PSTX\ vs.\ trans\ PST1}$ (for PSTX = 4, 7, 27) against experimental binding-affinity differences inferred from EC_{50} measurements (eq 5). We also compared the calculated $\Delta\Delta\Delta G_{PSTX\rightarrow PST1,\ cis\ vs.\ trans\ binding}$ for each PSTX−PST1 pair to the corresponding experimental values. These two complementary benchmarks provide a rigorous test of our methodology's robustness. Moreover, in doing so we gain molecular-level insights into the light-responsive protein−ligand interactions in these complex systems where experimental data are sparse or not easily interpreted by simple docking studies.

Table 5 compares the theoretical $\Delta\Delta\Delta G_{PSTX\rightarrow PST1,\ cis\ vs.\ trans\ binding}$ values with experimental re-

Table 5. Difference in the *Cis*-vs.-*Trans* Binding Free Energy Contrast (in kcal/mol) between PSTX and PST1 ($\Delta\Delta\Delta G_{PSTX\rightarrow PST1,cis\ vs.\ trans\ binding}$), with PSTX being PST7, PST27, and PST4, as Calculated by the TI Simulations[a]

Quantity	Simulation	Experiment
$\Delta\Delta\Delta G_{PST7\rightarrow PST1,\ cis\ vs.\ trans\ binding}$	2.3 ± 0.3	0.3 ± 0.4 (ref 24)
$\Delta\Delta\Delta G_{PST27\rightarrow PST1,\ cis\ vs.\ trans\ binding}$	-0.9 ± 0.7	≥ -0.81 (ref 27)
$\Delta\Delta\Delta G_{PST4\rightarrow PST1,\ cis\ vs.\ trans\ binding}$	-0.8 ± 0.1	-0.54 (ref 27)

[a]A positive $\Delta\Delta\Delta G$ value indicates higher *cis*-vs.-*trans* binding affinity contrast in PSTX than PST1.

Table 6. Difference in the Binding Free Energy (in kcal/mol) between PSTX and PST1 in the *Cis* and *Trans* Isomer Forms ($\Delta\Delta G_{binding,\ cis\ PSTX\ vs.\ cis\ PST1}$ and $\Delta\Delta G_{binding,\ trans\ PSTX\ vs.\ trans\ PST1}$), with PSTX being PST7, PST27, and PST4, as Calculated by the TI Simulations[a]

Quantity	Simulation	Experiment
$\Delta\Delta G_{binding,\ cis\ PST7\ vs.\ cis\ PST1}$	0.5 ± 0.3	0.2 ± 0.2 (ref 24)
$\Delta\Delta G_{binding,\ trans\ PST7\ vs.\ trans\ PST1}$	-1.8 ± 0.1	-0.1 ± 0.4 (ref 24)
$\Delta\Delta G_{binding,\ cis\ PST27\ vs.\ cis\ PST1}$	-0.6 ± 0.4	-0.76 (ref 27)
$\Delta\Delta G_{binding,\ trans\ PST27\ vs.\ trans\ PST1}$	0.3 ± 0.6	≤ 0.05 (ref 27)
$\Delta\Delta G_{binding,\ cis\ PST4\ vs.\ cis\ PST1}$	-1.4 ± 0.1	-0.61 (ref 27)
$\Delta\Delta G_{binding,\ trans\ PST4\ vs.\ trans\ PST1}$	-0.6 ± 0.1	-0.07 (ref 27)

[a]A positive $\Delta\Delta G_{binding}$ indicates a higher binding affinity of PSTX than PST1.

sults. Table 6 summarizes the theoretical and experimental relative binding free energies ($\Delta\Delta G_{binding,\ cis\ PSTX\ vs.\ cis\ PST1}$) for the three pairs of PSTs: PST7 vs. PST1, PST27 vs. PST1, and PST4 vs. PST1.

PST7 vs. PST1. Compared to PST1, PST7 has only one additional methylene moiety ($-CH_2-$) on the R_3 group of ring B (Figure 1B). A previous experimental study[24] reported that the *cis* PST7 has a lower EC_{50} than the *cis* PST1, translating to ~0.2 ± 0.2 kcal/mol stronger binding affinity than the latter (Table 6). The *trans* PST7, however, has a higher EC_{50} than the *trans* PST1, translating to 0.1 ± 0.4 kcal/mol weaker binding affinity than the latter (Table 6). Thus, the *cis*-vs.-*trans* binding affinity contrast was experimentally estimated to decrease by ~0.3 kcal/mol upon changing from PST7 to PST1. Our TI calculations are consistent with this trend semiquantitatively. Upon changing from PST7 to PST1,

the *cis*-vs.-*trans* binding affinity difference decreased by 2.3 ± 0.3 kcal/mol (Table 5, $\Delta\Delta\Delta G_{PST7\rightarrow PST1, \, cis \, vs. \, trans \, binding}$). These results suggest that PST7 undergoes a more significant increase in binding affinity upon *trans*-to-*cis* photoisomerization than PST1, consistent with its enhanced light-induced changes in bioactivity.[24] Additionally, the simulation accurately predicts the trends in relative binding affinity between the two PSTs in both isomeric forms ($\Delta\Delta G_{binding}$, Table 6). It is noteworthy that although our TI simulation results quantitatively differ from the experiment, they correctly predict the qualitative trend. Simple docking simulations[24] and MM/PBSA simulations (see below) cannot predict either this qualitative trend, i.e., the *cis*-vs.-*trans* binding affinity contrast, or the binding affinity difference between the *cis* isomers of the two compounds. The difficulty in computational prediction lies in the minimal change in the substituent group. Thus, this result is significant in that it confirms the predictive power of TI to capture the nuanced substituents' effects on not only the absolute binding affinity of the same isomer but also the binding affinity contrast between different isomeric forms of the same ligand. The good prediction accuracy is achieved even when the substitution pattern is only minimally modified, which has been a very challenging task in photopharmacology.[5]

PST27 vs. PST1. The PST27 molecule has three methoxy groups on both rings A & B (R_1, R_2, and R_3) of PST1 replaced with three alkyl groups (Figure 1B). In another study,[27] the EC_{50} of *cis* PST27 was measured to be higher than *cis* PST1, indicating a weaker binding affinity of the former than the latter by ~0.76 kcal/mol (Table 6). The TI calculations indicate that *cis* PST1 binds tubulin more strongly than *cis* PST27 by 0.6 ± 0.4 (Table 6), consistent with the experimental data. The EC_{50} of *trans* PST27 was measured to be greater than 35 μM, but without a definite value, and the EC_{50} of *trans* PST1 was determined to be 38 μM. Thus, experimental data suggest that the *trans* PST27 most likely has a slightly higher binding affinity than *trans* PST1. Consistent with experimental data, our TI calculations indicate that *trans* PST27's binding affinity is slightly higher than *trans* PST1 by ~0.3 ± 0.6 kcal/mol. The TI simulations predict that the *cis*-vs.-*trans* binding affinity contrast in PST1 is higher than PST27 by ~0.9 ± 0.7 kcal/mol (Table 5), and the experiment indicates this quantity to be less than 0.81 kcal/mol. Thus, these simulation results are in quantitative agreement with experiments and provide insight into the incomplete experimental data. They confirm the trend that PST1 not only has a stronger binding affinity in *cis* isomer form but also a larger light-responsive binding affinity change than PST27.

PST4 vs. PST1. PST4 replaces one hydroxyl group on ring B of PST1 (R_4 group) with a single hydrogen atom (Figure 1B). Estimated from experimental data,[27] *cis* PST1 binds more strongly than *cis* PST4 by 0.61 kcal/mol, but *trans* PST1 binds marginally stronger than *trans* PST4 by 0.08 kcal/mol. Our calculated relative binding affinities are in excellent agreement with the experiments (Table 6). Also, the PST1 has a larger *cis*-vs.-*trans* binding affinity contrast than PST4 in both experiment and simulation (Table 5). These results indicate that converting PST1 to PST4 lowers both the binding affinity and the *cis*-vs.-*trans* binding affinity contrast. The decrease in binding affinity upon converting PST1 to PST4 is expected, since the −OH group in PST1 is hydrogen-bonded with the Thr179 residue in the α subunit (Figure 8A), which is broken by putting a hydrogen atom at the same position (Figure 8B). However, the change in the *cis*-vs.-*trans* binding affinity
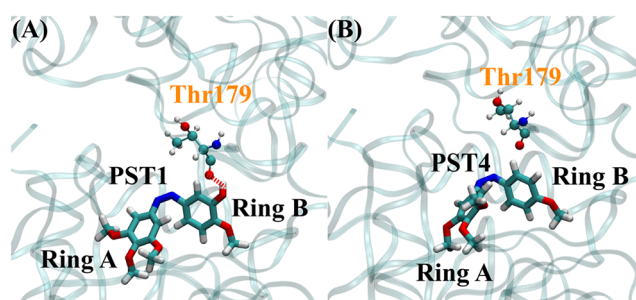
Figure 8. Equilibrated structures of (A) PST1, (B) PST4 at the tubulin dimer interface. The PSTs are depicted in licorice representation. The Thr179 residue in each structure is depicted as stick-and-ball representation. In PST1, a hydroxyl group on ring B forms a strong hydrogen bond with the Thr179, whereas in PST4, this hydrogen bond is absent.

contrast is far from obvious based on chemical intuition without quantitative free energy calculation, again highlighting the unique advantage of TI and alchemical free energy methods in predicting the substituents' effects on the light-responsiveness of bioactivity for this challenging class of photoswitches.

Furthermore, we benchmarked the MM/PBSA method for predicting the *cis*-vs.-*trans* binding affinity contrast in PST1 and PST7, using the final 100 ns of the production trajectories. The calculated binding free energies for PST1 were $\Delta G_{binding, \, cis \, PST1}$ = −39.50 kcal/mol (*cis* isomer) and $\Delta G_{binding, \, trans \, PST1}$ = −36.73 kcal/mol (*trans* isomer), resulting in a *cis*-vs.-*trans* binding free energy difference of $\Delta\Delta G_{PST1, \, trans \, vs. \, cis}$ = $\Delta G_{binding, \, cis \, PST1}$ − $\Delta G_{binding, \, trans \, PST1}$ = −2.77 kcal/mol. For PST7, MM/PBSA method predicted $\Delta G_{binding, \, cis \, PST7}$ = −42.78 kcal/mol (*cis* isomer) and $\Delta G_{binding, \, trans \, PST7}$ = −42.18 kcal/mol (*trans* isomer), resulting in a *cis*-vs.-*trans* binding free energy difference of $\Delta\Delta G_{PST7, \, trans \, vs. \, cis}$ = −0.6 kcal/mol. These values suggest that, in both molecules, the *cis* isomer binds more strongly than trans isomer, but the *cis*-vs.-*trans* binding free energy difference is substantially smaller in PST7 than PST1, *opposite to the trend observed in the experiment* (Table 5).

Additionally, we tested the MM/PBSA method's accuracy in estimating the relative binding affinities of PST7 to PST1 in the same isomeric form. In the *cis* form, PST7 exhibited a stronger binding affinity relative to PST1 ($\Delta\Delta G_{binding, \, cis \, PST7 \, vs. \, cis \, PST1}$ = 3.28 kcal/mol). A similar trend was observed for the trans isomer, with PST7 again showing stronger binding affinity ($\Delta\Delta G_{binding, \, cis \, PST7 \, vs. \, cis \, PST1}$ = 5.45 kcal/mol). These results are in line with the above-mentioned observations that PST7, overall, binds more tightly to the receptor in both conformations. However, when we compared these computational results to experimental values (Table 6), discrepancies were observed. Experimentally, the $\Delta\Delta G_{binding}$ between PST7 and PST1 was reported to be 0.2 kcal/mol for the *cis* form and −0.1 kcal/mol for the *trans* form. While the trend of PST7 binding more strongly than PST1 is correctly predicted by the MM/PBSA method, but the trend of *trans* PST7 binding more weakly than PST1 is not. Additionally, the magnitude of these relative differences is significantly overestimated by the MM/PBSA method, in contrast to the TI.

This inconsistency highlights a limitation of the MM/PBSA approach in photopharmacology. While it is computationally efficient and useful for estimating relative binding free energies of structurally very different compounds, it often lacks the accuracy required to reliably reproduce subtle experimental

M

trends, particularly when comparing structurally similar ligands or the same ligand in different conformational states. The reason is perhaps that the MM/PBSA simplifies solvation effects and entropy contributions, and it does not account for conformational sampling as accurately as alchemical free energy methods. In contrast, TI offers a more accurate and rigorous approach for calculating relative binding free energies by explicitly computing the free energy difference between the end states. Thus, the TI can better capture small changes in binding affinity for the selected compounds in this study.

Methodological Considerations in Spectra Calculations and Non-Adiabatic Dynamics. The hh-TDA method introduces further approximation to the particle−particle random phase approximation (pp-RPA) method.[68−71] The pp-RPA method's eigenvalue problem includes both the particle−particle and hole−hole channels. It allows the flexibility to use either the (N + 2)-electron system and (N − 2)-electron system as a reference for calculating both the ground and excited states of the N-electron system on equal footing, enabling the correct description of the conical intersection seam between the S_0 and S_1 states.[68] In the pp-RPA method, the particle−particle and hole−hole channels are coupled, and the TDA approximation decouples these two channels, generating the hh-TDA and pp-TDA methods. The hh-TDA method can only use the (N + 2)-electron system as the nonground-state reference, and the pp-TDA method can only use the (N − 2)-electron system as the nonground-state reference. In principle, the neglect of the coupling between the particle−particle and hole−hole channels in the hh-TDA or pp-TDA methods is an additional approximation, which could lead to less accurate results compared to pp-RPA. However, as discussed in ref 35, the full pp-RPA method may suffer from numerical instability due to the complex solutions to the eigenvalue problem near the conical intersections, and the hh-TDA method could be more robust and stable for on-the-fly PES calculations during the nonadiabatic dynamics simulations. Additionally, the current implementation of hh-TDA in TeraChem package, as used in this study, employed a functional-specific response kernel where the scaling factors of exact exchange integrals of the underlying hybrid functionals are built in.[35] This implementation differs from the original implementation, which uses a Hartree−Fock-type response kernel without the functional-specific parameters.[71] Therefore, further benchmark of hh-TDA vs pp-RPA method in this relatively new implementation is necessary to comprehensively evaluate their accuracy and stability in the context of nonadiabatic dynamics.

To generate ICs in the Franck−Condon region for the AIMS and absorption calculations, we sampled the configurations using ground-state QM/MM classical MD simulations. This step aims to ensure that a consistent Hamiltonian is used for both conformational sampling, absorption spectra calculation, and nonadiabatic dynamics simulations. Because both AIMS and absorption spectra employ the hh-TDA-BH&HLYP method to describe the PST's PES, it is essential to sample the structures near the FC point with a consistent Hamiltonian. Although using classical MD simulations with our parametrized force field of the PST ligand enabled efficient conformational sampling, it is still essential to equilibrate the ligands with an appropriate QM method for more precisely sampling the ground-state distribution of the ligand. This is because key internal coordinates, such as bond length alternation between single and double bonds, angles, and torsions, can affect the electronic structure, including π-electron delocalization, and the S_0-S_n energy gap and oscillator strengths. The distribution of these coordinates is sensitive to the Hamiltonian used for sampling. Because the hh-TDA-DFT is in good agreement with the much faster ground-state DFT calculations near the FC region,[35] provided that the same density functional is used, we employed ground-state QM/MM MD simulations with ground-state DFT as the QM method.

This approach sampled the structures of the full system according to the Boltzmann distribution, where the nuclear quantum effects, such as zero-point energies (ZPE), were neglected. Similar approaches, which do not account for ZPE effects in ground-state sampling, have been widely adopted in many simulation studies of photoactive biomolecules involving photoswitches,[13,14,34,72−82] including rhodopsins. Including the ZPE effects in the condensed-phase system using the Wigner sampling approach is a challenging task, since there are many slow and flexible modes with pronounced anharmonicity, making the application of Wigner sampling problematic.[83−87] Moreover, considering that the TBFs in the AIMS simulations mostly follow the classical dynamics, the added ZPE may not be redistributed correctly among the nuclear modes during the dynamics simulation, leading to artificial ZPE leakage problems. For these reasons, we used the classical QM/MM dynamics to sample the Boltzmann distribution instead of Wigner Sampling to incorporate the nuclear quantum effects. We expect that adding the ZPE to the ground-state sampling could broaden the sampled distribution and the calculated absorption spectra, as well as accelerate the excited-state dynamics.

To test the robustness of our IC selection approach for AIMS simulation, we computed the absorption spectra using (1) all QM/MM frames sampled along the equilibration, and (2) only the last equilibrated frames for each of the QM/MM trajectories (Figure S10), i.e., the ICs used for the AIMS simulation. The spectra calculated from the 80 ICs almost cover the full range of the spectra calculated using the whole ensemble of structures of 80 trajectories (3000 structures), and the peak of the spectra was well reproduced. This indicates that the 80 ICs selected for the AIMS simulations are representative of the full ensemble of sampled ground-state geometries.

In order to evaluate the influence of conformational sampling on the calculated spectra, we further extended 10 of our ground-state QM/MM trajectories in both water and protein for another 3 ps, and saved all snapshots with 1 fs interval. We compare the following spectra, which are calculated using (1) 1 fs sampling interval, using 10 trajectories, (2) 10 fs sampling interval, using the same 10 trajectories, (3) 10 fs sampling interval, using all 80 trajectories, and (4) 10 fs sampling interval, using a single QM/MM trajectory. These comparisons were performed for both PST1 in the aqueous solution and in the protein. The results are shown in Figure S11. Evidently, increasing the sampling frequency by a factor of 10 (10 fs vs 1 fs time interval) does not significantly broaden the calculated spectra or shift the energy at maximum absorption. Thus, this data justifies the choice of a 10 fs interval in the calculation of the spectra.

Furthermore, we emphasize that our sampling of QM/MM snapshots was initiated from structures sampled during 80 ns of classical MD trajectory for each compound. This nano-second-scale classical sampling time is much longer than each

individual picosecond-scale QM/MM trajectory. Thus, this multiscale sampling approach combines classical MM and QM/MM dynamics, and it captures the long-time scale thermal fluctuations of the system with structural corrections at *ab initio* accuracy, as discussed in ref 34. This long-time configurational sampling across 80 ns is important, as indicated in the difference in the spectra calculated with snapshots sampled from only 1 QM/MM trajectory vs all trajectories (Figure S11). In contrast, changing the QM/MM snapshot frequency from 0.1 to 1 fs^{-1} makes a negligible difference to the width of the spectra and produces nearly identical lineshapes (Figure S11).

CONCLUSION

This study presents a systematic multiscale computational approach for computationally investigating the photo-SAR of light-responsive biomolecular systems, focusing on the PST-tubulin complex as a case study. By combining first-principles nonadiabatic dynamics simulations with excited- and ground-state free energy calculations, this multiscale approach can faithfully reproduce experimental measurements of the photo-dynamics and light-responsive binding affinities of the PSTs. The results validate its accuracy for modeling photochemical reactions and protein−ligand interactions in complex photo-active biomolecular systems.

Our results also provide unprecedented mechanistic insights into how substituent modifications and biomolecular environment can significantly influence excited-state relaxation dynamics, photoisomerization quantum yield, binding affinities with tubulin, and, importantly, the binding affinity contrasts between *cis* and *trans* isomers. Interestingly, even minor changes to the substituents can dramatically reshape the excited-state free energy landscape, which is discovered to be closely associated with the isomerization kinetics (Figures 4 and S1). For instance, replacing a methoxy group in PST1 with an ethoxy group in PST7 decelerates the nonradiative decay while also enhancing the binding affinity difference between the *cis* and *trans* isomers. Furthermore, the protein environment plays a crucial role in photodynamics through a combination of local electric fields and steric confinements, which facilitate and impede the main torsional modes leading to the vicinity of the conical intersection seam, respectively. Although a higher excitation energy (blue-shifted absorption spectrum) can lead to faster torsional velocity during a nonadiabatic transition (e.g., PST27), it does not necessarily translate to a higher quantum yield. The alignment between the atoms' velocities with the nonadiabatic coupling vector is an equally important factor determining the quantum efficiency in photoisomerization. This is a unique and important insight into the design principle, as revealed through nonadiabatic dynamic simulations, and it represents an important contribution from this study.

Our work also makes another key methodological contribution: for the first time, we benchmarked the TI method for quantifying the effects of substituents on the relative potency between different isomer forms of the photoswitches. This task has been computationally challenging for various widely used approaches, such as docking and MM/PBSA. Our work thus demonstrates the potential of alchemical free energy methods for accurately modeling small, yet functionally significant, perturbations in complex photoactive biomolecules.

Overall, our computational approach provides a generalizable strategy for simulating photoinduced reactions and binding selectivity of molecular photoswitches in realistic settings relevant to biological and biomedical applications. By integrating high-accuracy quantum mechanical, quantum dynamical, and free energy calculations, our multiscale computational framework advances our ability to mechanistically interpret and predict the behavior of light-responsive biomolecular systems at the atomic level.

ASSOCIATED CONTENT

Data Availability Statement

We refer the readers to the Supporting Information file for additional data related to the properties of the molecular systems investigated in this manuscript. The structures for the initial simulation setup of the PST-tubulin systems are included in the Structures.zip file.

Ⓢ Supporting Information

The Supporting Information is available free of charge at https://pubs.acs.org/doi/10.1021/acs.jcim.5c01831.

> The Supporting Information contains Figures S1−S11 and Tables S1−S6, as referenced throughout the main text. The tables include the gas-phase excitation energy benchmarks at XMS-CASPT2 level of theory, analysis of electric field created by different environments, conditional quantum yields, and alchemical free energy changes from TI calculations. The figures include correlations between slopes of PMFs, excited-state energy gap between FC point and MECI and relaxation time constants, geometric distribution of ICs, analysis of the population decay channels, comparison of UV−vis spectra, active space orbitals of XMS-CASPT2 calculations, QM/MM partitioning scheme, and S$_1$-state PES of PSTs (PDF)

> Structures for the initial simulation setup of the PST-tubulin systems (ZIP)

AUTHOR INFORMATION

Corresponding Author

Ruibin Liang − *Department of Chemistry and Biochemistry, Texas Tech University, Lubbock, Texas 79409, United States;* ⓞ orcid.org/0000-0001-8741-1520; Email: rliang@ttu.edu

Authors

Amirhossein Bakhtiiari − *Department of Chemistry and Biochemistry, Texas Tech University, Lubbock, Texas 79409, United States*

Mohammad Khavani − *Department of Chemistry and Biochemistry, Texas Tech University, Lubbock, Texas 79409, United States*

Gustavo J. Costa − *Department of Chemistry and Biochemistry, Texas Tech University, Lubbock, Texas 79409, United States*

Complete contact information is available at:
https://pubs.acs.org/10.1021/acs.jcim.5c01831

Author Contributions

Ruibin Liang designed the research project. Amirhossein Bakhtiiari, Mohammad Khavani, and Gustavo J. Costa performed the simulations and analyzed the data. Ruibin

Liang, Amirhossein Bakhtiiari, Mohammad Khavani, and Gustavo J. Costa wrote and revised the manuscript.

Notes

The authors declare no competing financial interest.

■ REFERENCES

(1) Szymański, W.; Beierle, J. M.; Kistemaker, H. A. V.; Velema, W. A.; Feringa, B. L. Reversible Photocontrol of Biological Systems by the Incorporation of Molecular Photoswitches. *Chem. Rev.* **2013**, *113* (8), 6114−6178.

(2) Broichhagen, J.; Frank, J. A.; Trauner, D. A Roadmap to Success in Photopharmacology. *Acc. Chem. Res.* **2015**, *48* (7), 1947−1960.

(3) Hüll, K.; Morstein, J.; Trauner, D. In Vivo Photopharmacology. *Chem. Rev.* **2018**, *118* (21), 10710−10747.

(4) Paoletti, P.; Ellis-Davies, G. C. R.; Mourot, A. Optical control of neuronal ion channels and receptors. *Nat. Rev. Neurosci.* **2019**, *20* (9), 514−532.

(5) Kobauri, P.; Dekker, F. J.; Szymanski, W.; Feringa, B. L. Rational Design in Photopharmacology with Molecular Photoswitches. *Angew. Chem., Int. Ed.* **2023**, *62* (30), No. e202300681.

(6) Frank, J. A.; Yushchenko, D. A.; Hodson, D. J.; Lipstein, N.; Nagpal, J.; Rutter, G. A.; Rhee, J.-S.; Gottschalk, A.; Brose, N.; Schultz, C.; Trauner, D. Photoswitchable diacylglycerols enable optical control of protein kinase C. *Nat. Chem. Biol.* **2016**, *12* (9), 755−762.

(7) Morstein, J.; Hill, R. Z.; Novak, A. J. E.; Feng, S.; Norman, D. D.; Donthamsetti, P. C.; Frank, J. A.; Harayama, T.; Williams, B. M.; Parrill, A. L.; et al. Optical control of sphingosine-1-phosphate formation and function. *Nat. Chem. Biol.* **2019**, *15* (6), 623−631.

(8) Borowiak, M.; Nahaboo, W.; Reynders, M.; Nekolla, K.; Jalinot, P.; Hasserodt, J.; Rehberg, M.; Delattre, M.; Zahler, S.; Vollmar, A.; et al. Photoswitchable Inhibitors of Microtubule Dynamics Optically Control Mitosis and Cell Death. *Cell* **2015**, *162* (2), 403−411.

(9) Sheldon, J. E.; Dcona, M. M.; Lyons, C. E.; Hackett, J. C.; Hartman, M. C. T. Photoswitchable anticancer activity via trans−cis isomerization of a combretastatin A-4 analog. *Org. Biomol. Chem.* **2016**, *14* (1), 40−49 10.1039/C5OB02005K..

(10) Babii, O.; Afonin, S.; Garmanchuk, L. V.; Nikulina, V. V.; Nikolaienko, T. V.; Storozhuk, O. V.; Shelest, D. V.; Dasyukevich, O. I.; Ostapchenko, L. I.; Iurchenko, V.; et al. Direct Photocontrol of Peptidomimetics: An Alternative to Oxygen-Dependent Photo-dynamic Cancer Therapy. *Angew. Chem., Int. Ed.* **2016**, *55* (18), 5493−5496.

(11) Matera, C.; Gomila, A. M. J.; Camarero, N.; Libergoli, M.; Soler, C.; Gorostiza, P. Photoswitchable Antimetabolite for Targeted Photoactivated Chemotherapy. *J. Am. Chem. Soc.* **2018**, *140* (46), 15764−15773.

(12) Liang, R.; Das, D.; Bakhtiiari, A. Protein confinement fine-tunes aggregation-induced emission in human serum albumin. *Phys. Chem. Chem. Phys.* **2021**, *23* (46), 26263−26272 10.1039/D1CP04577F..

(13) Liang, R.; Bakhtiiari, A. Multiscale simulation unravels the light-regulated reversible inhibition of dihydrofolate reductase by photo-trexate. *J. Chem. Phys.* **2022**, *156* (24), No. 245102.

(14) Liang, R.; Bakhtiiari, A. Effects of Enzyme−Ligand Interactions on the Photoisomerization of a Light-Regulated Chemotherapeutic Drug. *J. Phys. Chem. B* **2022**, *126* (12), 2382−2393.

(15) Glover, H.; Saßmannshausen, T.; Bertrand, Q.; Trabuco, M.; Slavov, C.; Bacchin, A.; Andres, F.; Kondo, Y.; Stipp, R.; Wranik, M.; et al. Photoswitch dissociation from a G protein-coupled receptor resolved by time-resolved serial crystallography. *Nat. Commun.* **2024**, *15* (1), No. 10837.

(16) Bakhtiiari, A.; Costa, G. J.; Liang, R. On the Simulation of Thermal Isomerization of Molecular Photoswitches in Biological Systems. *J. Chem. Theory Comput.* **2023**, *19* (18), 6484−6499.

(17) Reed, P. M. M.; Jang, J.; Woloschuk, R. M.; Reis, J.; Hille, J. I. C.; Uppalapati, M.; Woolley, G. A. Effects of binding partners on thermal reversion rates of photoswitchable molecules. *Proc. Natl. Acad. Sci. U.S.A.* **2025**, *122* (10), No. e2414748122.

(18) Hosseinizadeh, A.; Breckwoldt, N.; Fung, R.; Sepehr, R.; Schmidt, M.; Schwander, P.; Santra, R.; Ourmazd, A. Few-fs resolution of a photoactive protein traversing a conical intersection. *Nature* **2021**, *599* (7886), 697−701.

(19) Westenhoff, S.; Meszaros, P.; Schmidt, M. Protein motions visualized by femtosecond time-resolved crystallography: The case of photosensory vs photosynthetic proteins. *Curr. Opin. Struct. Biol.* **2022**, *77*, No. 102481.

(20) Wranik, M.; Weinert, T.; Slavov, C.; Masini, T.; Furrer, A.; Gaillard, N.; Gioia, D.; Ferrarotti, M.; James, D.; Glover, H.; et al. Watching the release of a photopharmacological drug from tubulin using time-resolved serial crystallography. *Nat. Commun.* **2023**, *14* (1), No. 903.

(21) Standfuss, J.; Weinert, T.; Wranik, M.; Church, J.; Seidel, H. P.; Slavov, C.; Masini, T.; James, D.; Glover, H.; Carrillo, M.et al. Direct observation of coherent azobenzene photochemistry. *Research Square* 2023, PREPRINT (Version 1) DOI: 10.21203/rs.3.rs-3490897/v1.

(22) Brändén, G.; Neutze, R. Advances and challenges in time-resolved macromolecular crystallography. *Science* **2021**, *373* (6558), No. eaba0954.

(23) Cederbaum, L. S.Born−Oppenheimer approximation and beyond. In *Conical Intersections: Electronic Structure, Dynamics and Spectroscopy*, Advanced Series in Physical Chemistry; World Scientific, 2004; Vol. 15, pp 3−40 .

(24) Rastogi, S. K.; Zhao, Z.; Barrett, S. L.; Shelton, S. D.; Zafferani, M.; Anderson, H. E.; Blumenthal, M. O.; Jones, L. R.; Wang, L.; Li, X.; et al. Photoresponsive azo-combretastatin A-4 analogues. *Eur. J. Med. Chem.* **2018**, *143*, 1−7.

(25) Kobauri, P.; Galenkamp, N. S.; Schulte, A. M.; de Vries, J.; Simeth, N. A.; Maglia, G.; Thallmair, S.; Kolarski, D.; Szymanski, W.; Feringa, B. L. Hypothesis-Driven, Structure-Based Design in Photo-pharmacology: The Case of eDHFR Inhibitors. *J. Med. Chem.* **2022**, *65* (6), 4798−4817.

(26) Pettit, G. R.; Singh, S. B.; Hamel, E.; Lin, C. M.; Alberts, D. S.; Garcia-Kendal, D. Isolation and structure of the strong cell growth and tubulin inhibitor combretastatin A-4. *Experientia* **1989**, *45* (2), 209−211.

(27) Reynders, M.; Garśica, M.; Müller-Deku, A.; Wranik, M.; Krauskopf, K.; de la Osa de la Rosa, L.; Schaffer, K.; Jötten, A.; Rode, A.; Stierle, V.; et al. A photo-SAR study of photoswitchable azobenzene tubulin-inhibiting antimitotics identifying a general method for near-quantitative photocontrol. *Chem. Sci.* **2024**, *15* (31), 12301−12309 10.1039/D4SC03072A..

(28) Ben-Nun, M.; Quenneville, J.; Martínez, T. J. Ab Initio Multiple Spawning: Photochemistry from First Principles Quantum Molecular Dynamics. *J. Phys. Chem. A* **2000**, *104* (22), 5161−5175.

(29) Ben-Nun, M.; Martínez, T. J. Ab Initio Quantum Molecular Dynamics. In *Advances in Chemical Physics*; John Wiley & Sons, Inc., 2002; pp 439−512.

(30) Curchod, B. F. E.; Martínez, T. J. Ab Initio Nonadiabatic Quantum Molecular Dynamics. *Chem. Rev.* **2018**, *118* (7), 3305−3336.

(31) Curchod, B. F. E.; Glover, W. J.; Martínez, T. J. SSAIMS—Stochastic-Selection Ab Initio Multiple Spawning for Efficient Nonadiabatic Molecular Dynamics. *J. Phys. Chem. A* **2020**, *124* (30), 6133−6143.

(32) Yu, J. K.; Bannwarth, C.; Liang, R.; Hohenstein, E. G.; Martínez, T. J. Nonadiabatic Dynamics Simulation of the Wavelength-Dependent Photochemistry of Azobenzene Excited to the $n\pi^*$ and $\pi\pi^*$ Excited States. *J. Am. Chem. Soc.* **2020**, *142* (49), 20680−20690.

(33) Liang, R. First-Principles Nonadiabatic Dynamics Simulation of Azobenzene Photodynamics in Solutions. *J. Chem. Theory Comput.* **2021**, *17* (5), 3019−3030.

(34) Bakhtiiari, A.; Liang, R. Unraveling Solvent and Substituent Effects in the Photodynamics of Light-Dependent Microtubule Inhibitors for Cancer Phototherapy. *J. Comput. Chem.* **2025**, *46* (7), No. e70076.

(35) Bannwarth, C.; Yu, J. K.; Hohenstein, E. G.; Martínez, T. J. Hole−hole Tamm−Dancoff-approximated density functional theory: A highly efficient electronic structure method incorporating dynamic and static correlation. *J. Chem. Phys.* **2020**, *153* (2), No. 024110.

(36) Webb, B.; Sali, A. Comparative Protein Structure Modeling Using MODELLER. *Curr. Protoc. Bioinform.* **2016**, *54* (1), 5.6.1−5.6.37.

(37) Anandakrishnan, R.; Aguilar, B.; Onufriev, A. V. H++ 3.0: automating p K prediction and the preparation of biomolecular structures for atomistic molecular modeling and simulations. *Nucleic Acids Res.* **2012**, *40* (W1), W537−W541.

(38) Case, D. A.; Aktulga, H. M.; Belfon, K.; Cerutti, D. S.; Cisneros, G. A.; Cruzeiro, V. W. D.; Forouzesh, N.; Giese, T. J.; Götz, A. W.; Gohlke, H.; et al. AmberTools. *J. Chem. Inf. Model.* **2023**, *63* (20), 6183−6191.

(39) Maier, J. A.; Martinez, C.; Kasavajhala, K.; Wickstrom, L.; Hauser, K. E.; Simmerling, C. ff14SB: Improving the Accuracy of Protein Side Chain and Backbone Parameters from ff99SB. *J. Chem. Theory Comput.* **2015**, *11* (8), 3696−3713.

(40) Dickson, C. J.; Madej, B. D.; Skjevik, Å. A.; Betz, R. M.; Teigen, K.; Gould, I. R.; Walker, R. C. Lipid14: The Amber Lipid Force Field. *J. Chem. Theory Comput.* **2014**, *10* (2), 865−879.

(41) Wu, Y.; Tepper, H. L.; Voth, G. A. Flexible simple point-charge water model with improved liquid-state properties. *J. Chem. Phys.* **2006**, *124* (2), No. 024503.

(42) Wang, J.; Wolf, R. M.; Caldwell, J. W.; Kollman, P. A.; Case, D. A. Development and testing of a general amber force field. *J. Comput. Chem.* **2004**, *25* (9), 1157−1174.

(43) Wang, J.; Wang, W.; Kollman, P. A.; Case, D. A. Automatic atom type and bond type perception in molecular mechanical calculations. *J. Mol. Graphics Modell.* **2006**, *25* (2), 247−260.

(44) Meagher, K. L.; Redman, L. T.; Carlson, H. A. Development of polyphosphate parameters for use with the AMBER force field. *J. Comput. Chem.* **2003**, *24* (9), 1016−1025.

(45) Bakhtiiari, A.; Liang, R. Unraveling solvent and substituent effects in the photodynamics of light-dependent microtubule inhibitors for cancer phototherapy. *J. Comput. Chem.* **2024**, *46* (7), No. e70076, DOI: 10.1002/jcc.70076.

(46) Case, D. A.; Belfon, K.; Ben-Shalom, I. Y.; Brozell, S. R.; Cerutti, D. S.; Cheatham, T. E., III; Cruzeiro, V. W. D.; Darden, T. A.; Duke, R. E.; Giambasu, G.et al. *AMBER 2020*; University of California: San Francisco, 2020.

(47) Darden, T.; York, D.; Pedersen, L. Particle mesh Ewald: An N log (N) method for Ewald sums in large systems. *J. Chem. Phys.* **1993**, *98*, 10089−10089.

(48) Ufimtsev, I. S.; Martinez, T. J. Quantum Chemistry on Graphical Processing Units. 3. Analytical Energy Gradients, Geometry Optimization, and First Principles Molecular Dynamics. *J. Chem. Theory Comput.* **2009**, *5* (10), 2619−2628.

(49) Titov, A. V.; Ufimtsev, I. S.; Luehr, N.; Martinez, T. J. Generating Efficient Quantum Chemistry Codes for Novel Architectures. *J. Chem. Theory Comput.* **2013**, *9* (1), 213−221.

(50) Seritan, S.; Bannwarth, C.; Fales, B. S.; Hohenstein, E. G.; Kokkila-Schumacher, S. I. L.; Luehr, N.; Snyder, J. W., Jr.; Song, C.; Titov, A. V.; Ufimtsev, I. S.; Martínez, T. J. TeraChem: Accelerating electronic structure and ab initio molecular dynamics with graphical processing units. *J. Chem. Phys.* **2020**, *152* (22), No. 224110.

(51) Seritan, S.; Bannwarth, C.; Fales, B. S.; Hohenstein, E. G.; Isborn, C. M.; Kokkila-Schumacher, S. I. L.; Li, X.; Liu, F.; Luehr, N.; Snyder, J. W., Jr; et al. TeraChem: A graphical processing unit-accelerated electronic structure package for large-scale ab initio molecular dynamics. *Wiley Interdiscip. Rev.: Comput. Mol. Sci.* **2021**, *11* (2), No. e1494.

(52) Seritan, S.; Bannwarth, C.; Fales, B. S.; Hohenstein, E. G.; Kokkila-Schumacher, S. I.; Luehr, N.; Snyder, J. W.; Song, C.; Titov, A. V.; Ufimtsev, I. S.; Martínez, T. J. TeraChem: Accelerating electronic structure and ab initio molecular dynamics with graphical processing units. *J. Chem. Phys.* **2020**, *152* (22), No. 224110, DOI: 10.1063/5.0007615.

(53) Seritan, S.; Bannwarth, C.; Fales, B. S.; Hohenstein, E. G.; Isborn, C. M.; Kokkila-Schumacher, S. I.; Li, X.; Liu, F.; Luehr, N.; Snyder, J. W., Jr; et al. TeraChem: A graphical processing unit-accelerated electronic structure package for large-scale ab initio molecular dynamics. *Wiley Interdiscip. Rev.: Comput. Mol. Sci.* **2021**, *11* (2), No. e1494.

(54) Jones, C. M.; List, N. H.; Martínez, T. J. Steric and Electronic Origins of Fluorescence in GFP and GFP-like Proteins. *J. Am. Chem. Soc.* **2022**, *144* (28), 12732−12746.

(55) Eastman, P.; Friedrichs, M. S.; Chodera, J. D.; Radmer, R. J.; Bruns, C. M.; Ku, J. P.; Beauchamp, K. A.; Lane, T. J.; Wang, L.-P.; Shukla, D.; et al. OpenMM 4: A Reusable, Extensible, Hardware Independent Library for High Performance Molecular Simulation. *J. Chem. Theory Comput.* **2013**, *9* (1), 461−469.

(56) Barbatti, M.; Aquino, A. J.; Lischka, H. The UV absorption of nucleobases: semi-classical ab initio spectra simulations. *Phys. Chem. Chem. Phys.* **2010**, *12* (19), 4959−4967.

(57) Bonomi, M.; Branduardi, D.; Bussi, G.; Camilloni, C.; Provasi, D.; Raiteri, P.; Donadio, D.; Marinelli, F.; Pietrucci, F.; Broglia, R. A.; Parrinello, M. PLUMED: A portable plugin for free-energy calculations with molecular dynamics. *Comput. Phys. Commun.* **2009**, *180* (10), 1961−1972.

(58) Shiozaki, T.; Győrffy, W.; Celani, P.; Werner, H.-J. Communication: Extended multi-state complete active space second-order perturbation theory: Energy and nuclear gradients. *J. Chem. Phys.* **2011**, *135* (8), No. 081106.

(59) Finley, J.; Malmqvist, P.-Å.; Roos, B. O.; Serrano-Andrés, L. The multi-state CASPT2 method. *Chem. Phys. Lett.* **1998**, *288* (2), 299−306.

(60) Andersson, K.; Malmqvist, P.-Å.; Roos, B. O. Second-order perturbation theory with a complete active space self-consistent field reference function. *J. Chem. Phys.* **1992**, *96* (2), 1218−1226.

(61) Andersson, K.; Malmqvist, P. A.; Roos, B. O.; Sadlej, A. J.; Wolinski, K. Second-order perturbation theory with a CASSCF reference function. *J. Phys. Chem. A* **1990**, *94* (14), 5483−5488.

(62) Yu, J. K.; Bannwarth, C.; Hohenstein, E. G.; Martínez, T. J. Ab initio nonadiabatic molecular dynamics with hole−hole Tamm−Dancoff approximated density functional theory. *J. Chem. Theory Comput.* **2020**, *16* (9), 5499−5511.

(63) Shiozaki, T. BAGEL: Brilliantly Advanced General Electronic-structure Library. *Wiley Interdiscip. Rev.: Comput. Mol. Sci.* **2018**, *8* (1), No. e1331.

(64) *BAGEL, Brilliantly Advanced General Electronic-structure Library*. http://www.nubakery.org under the GNU General Public License.

(65) Lu, Q.; Luo, R. A Poisson−Boltzmann dynamics method with nonperiodic boundary condition. *J. Chem. Phys.* **2003**, *119* (21), 11035−11047.

(66) Miller, B. R.; McGee, T. D., Jr; Swails, J. M.; Homeyer, N.; Gohlke, H.; Roitberg, A. E. MMPBSA. py: an efficient program for end-state free energy calculations. *J. Chem. Theory Comput.* **2012**, *8* (9), 3314−3321.

(67) Kingsland, A.; Samai, S.; Yan, Y.; Ginger, D. S.; Maibaum, L. Local Density Fluctuations Predict Photoisomerization Quantum Yield of Azobenzene-Modified DNA. *J. Phys. Chem. Lett.* **2016**, *7* (15), 3027−3031.

(68) Yang, Y.; van Aggelen, H.; Yang, W. Double, Rydberg and charge transfer excitations from pairing matrix fluctuation and

Q

particle-particle random phase approximation. *J. Chem. Phys.* **2013**, *139* (22), No. 224105.

(69) Yu, J.; Li, J.; Zhu, T.; Yang, W. Accurate and efficient prediction of double excitation energies using the particle−particle random phase approximation. *J. Chem. Phys.* **2025**, *162* (9), No. 094101.

(70) Yang, Y.; Peng, D.; Lu, J.; Yang, W. Excitation energies from particle-particle random phase approximation: Davidson algorithm and benchmark studies. *J. Chem. Phys.* **2014**, *141* (12), No. 124104.

(71) Peng, D.; van Aggelen, H.; Yang, Y.; Yang, W. Linear-response time-dependent density-functional theory with pairing fields. *J. Chem. Phys.* **2014**, *140* (18), No. 18A522.

(72) Liang, R.; Liu, F.; Martínez, T. J. Nonadiabatic Photodynamics of Retinal Protonated Schiff Base in Channelrhodopsin 2. *J. Phys. Chem. Lett.* **2019**, *10* (11), 2862−2868.

(73) Liang, R.; Yu, J. K.; Meisner, J.; Liu, F.; Martinez, T. J. Electrostatic Control of Photoisomerization in Channelrhodopsin 2. *J. Am. Chem. Soc.* **2021**, *143* (14), 5425−5437.

(74) Gozem, S.; Luk, H. L.; Schapiro, I.; Olivucci, M. Theory and Simulation of the Ultrafast Double-Bond Isomerization of Biological Chromophores. *Chem. Rev.* **2017**, *117*, 13502.

(75) Yang, X.; Manathunga, M.; Gozem, S.; Léonard, J.; Andruniów, T.; Olivucci, M. Quantum−classical simulations of rhodopsin reveal excited-state population splitting and its effects on quantum efficiency. *Nat. Chem.* **2022**, *14* (4), 441−449.

(76) Yu, J. K.; Liang, R.; Liu, F.; Martínez, T. J. First-Principles Characterization of the Elusive I Fluorescent State and the Structural Evolution of Retinal Protonated Schiff Base in Bacteriorhodopsin. *J. Am. Chem. Soc.* **2019**, *141* (45), 18193−18203.

(77) Polli, D.; Altoè, P.; Weingart, O.; Spillane, K. M.; Manzoni, C.; Brida, D.; Tomasello, G.; Orlandi, G.; Kukura, P.; Mathies, R. A.; et al. Conical intersection dynamics of the primary photoisomerization event in vision. *Nature* **2010**, *467*, 440.

(78) El-Tahawy, M. M. T.; Nenov, A.; Weingart, O.; Olivucci, M.; Garavelli, M. Relationship between Excited State Lifetime and Isomerization Quantum Yield in Animal Rhodopsins: Beyond the One-Dimensional Landau−Zener Model. *J. Phys. Chem. Lett.* **2018**, *9* (12), 3315−3322.

(79) Malakar, P.; Gholami, S.; Aarabi, M.; Rivalta, I.; Sheves, M.; Garavelli, M.; Ruhman, S. Retinal photoisomerization versus counterion protonation in light and dark-adapted bacteriorhodopsin and its primary photoproduct. *Nat. Commun.* **2024**, *15* (1), No. 2136.

(80) Martínez, T. J. Insights for Light-Driven Molecular Devices from Ab Initio Multiple Spawning Excited-State Dynamics of Organic and Biological Chromophores. *Acc. Chem. Res.* **2006**, *39* (2), 119−126.

(81) Punwong, C.; Martínez, T. J.; Hannongbua, S. Direct QM/MM simulation of photoexcitation dynamics in bacteriorhodopsin and halorhodopsin. *Chem. Phys. Lett.* **2014**, *610−611* (Supplement C), 213−218.

(82) Punwong, C.; Hannongbua, S.; Martínez, T. J. Electrostatic Influence on Photoisomerization in Bacteriorhodopsin and Halorhodopsin. *J. Phys. Chem. B* **2019**, *123* (23), 4850−4857.

(83) Mai, S.; Gattuso, H.; Monari, A.; González, L. Novel molecular-dynamics-based protocols for phase space sampling in complex systems. *Front. Chem.* **2018**, *6*, 495.

(84) McCoy, A. B. The role of electrical anharmonicity in the association band in the water spectrum. *J. Phys. Chem. B* **2014**, *118* (28), 8286−8294.

(85) Persico, M.; Granucci, G. An overview of nonadiabatic dynamics simulations methods, with focus on the direct approach versus the fitting of potential energy surfaces. *Theor. Chem. Acc.* **2014**, *133* (9), 1526.

(86) Prlj, A.; Hollas, D.; Curchod, B. F. Deciphering the influence of ground-state distributions on the calculation of photolysis observables. *J. Phys. Chem. A* **2023**, *127* (35), 7400−7409.

(87) Suchan, J.; Hollas, D.; Curchod, B. F.; Slavíček, P. On the importance of initial conditions for excited-state dynamics. *Faraday Discuss.* **2018**, *212*, 307−330.